Degradation of fast-ion confinement depending on the neutral beam power in MHD quiescent LHD plasmas

メタデータ	言語: en
	出版者: IOP Publishing
	公開日: 2024-04-24
	キーワード (Ja):
	キーワード (En):
	作成者: NUGA, Hideo, SEKI, Ryosuke, OGAWA, Kunihiro, YAMAGUCHI, Hiroyuki, KAMIO, Shuji, FUJIWARA, Yutaka, KAWAMOTO, Yasuko, YOSHINUMA, Mikirou, KOBAYASHI, Tatsuya, TAKEMURA, Yuuki, ISOBE, Mitsutaka, OSAKABE, Masaki, YOKOYAMA, Masayuki
	メールアドレス:
	所属:
URL	http://hdl.handle.net/10655/0002000558

Degradation of fast-ion confinement depending on the neutral beam power in MHD quiescent LHD plasmas

View the article online for updates and enhancements.

Degradation of fast-ion confinement depending on the neutral beam power in MHD quiescent LHD plasmas

H. Nuga[1,*] ![ORCID], **R. Seki**[1] ![ORCID], **K. Ogawa**[1,2] ![ORCID], **H. Yamaguchi**[1,2] ![ORCID], **S. Kamio**[3] ![ORCID], **Y. Fujiwara**[3] ![ORCID], **Y. Kawamoto**[1,2] ![ORCID], **M. Yoshinuma**[1] ![ORCID], **T. Kobayashi**[1,2] ![ORCID], **Y. Takemura**[1] ![ORCID], **M. Isobe**[1,2] ![ORCID], **M. Osakabe**[1,2] ![ORCID] and **M. Yokoyama**[1,2] ![ORCID]

[1] National Institute for Fusion Science, National Institutes of Natural Sciences, Toki, Japan
[2] The Graduate University for Advanced Studies, SOKENDAI, Toki, Japan
[3] University of California, Irvine, CA, United States of America

E-mail: nuga.hideo@nifs.ac.jp

Abstract

We investigated the degradation of neutral beam (NB) fast-ion confinement depending on the NB power without magnetohydrodynamics instabilities in the Large Helical Device (LHD). In the LHD deuterium experiment, the neutron emission rate per NB power decreased by up to 20% with increasing injected NBs during a single discharge. Because there were no significant variations in the electron temperature and density, the NB shine-through rate, or the magnetic fluctuation due to the change in NB power, the reduction in the neutron emission rate indicates the degradation of the fast-ion confinement. In this paper, we formulated this degradation depending on the NB power and quantitatively estimated the degraded effective confinement time. In addition, we performed neutron emission rate simulations using the obtained effective confinement time. The simulation and experimental results were in good agreement, suggesting that the degraded effective confinement time is valid.

Keywords: fast-ion confinement, Fokker–Planck, neutron emission rate

(Some figures may appear in colour only in the online journal)

1. Introduction

In magnetically confined fusion devices, the high confinement of fast-ions, which are generated by fusion reactions, neutral beam injections (NBIs), and radio frequency (RF) waves, is necessary in nuclear fusion power plants because the economic efficiency of such power plant. However, before the

fast-ion kinetic energy is lost due to the collision, fast-ions are often lost from the confined plasma due to various confinement degradation effects. Therefore, many researchers have investigated degradation mechanisms and the methods to suppress them [1, 2].

Fast-ion-driven magnetohydrodynamic (MHD) instabilities can cause fast-ion loss. One of the most essential features of this kind of loss is that the fast-ion transport coefficient depends on the NB power [3] in contrast to the neo-classical transport and charge exchange (CX) losses. This is because the amplitude of the fast-ion-driven instability depends on the fast-ion pressure. Therefore, MHD instabilities lead to the degradation fast-ion confinement with increasing NB power.

---

* Author to whom any correspondence should be addressed.

For the first deuterium plasma experiments with the Large Helical Device (LHD) performed in 2017 [4–7], neutron measurement systems were installed [8–11] in the LHD. Neutron measurement systems are important tools in the fast-ion confinement studies. The neutron emission rate reflects fast-ion confinement since the deuterium–deuterium (DD) fusion reaction between a fast-deuteron and a thermal-deuteron dominates in the LHD.

In our previous study [12, 13], the effective fast-ion confinement time was estimated by measurements with the neutron flux monitor [10] and integrated simulations with TASK3D-a [14]. In addition, we clarified that neo-classical transport does not dominate the NB fast-ion loss in the LHD [15], especially for tangential NB fast-ions. In these works, short-pulse (∼40 ms) NB injection experiments were performed to suppress the fast-ion-driven instabilities and the variation in the plasma parameters. In typical LHD experiments, however, the NB injections are 2 seconds for each beam. Therefore, whether the obtained effective confinement time can be adapted for typical LHD discharges remains unclear.

In this paper, we investigate the degradation of fast-ion confinement depending on the NB power observed in MHD quiescent LHD plasmas. In these discharges, the plasmas reach a steady state with electron cyclotron heating (ECH) and NBIs. The degraded effective confinement time is quantitatively estimated. In addition, the dependency of the degradation on the plasma density is investigated.

The remainder of this paper is structed as follows. The experimental apparatus and the experimental scenario are presented in section 2. The experimental results are introduced in section 3. The confinement degradation analytical model is formulated and the degraded confinement times are estimated in section 3.1. According to the estimated confinement time, neutron emission rate simulation are performed in section 4. The NB heating efficiency and the degradation mechanism are discussed in section 5. Section 6 concludes this paper. The details of the neutron emission rate simulation are provided in appendix A.

2. Experimental set-up

2.1. Experimental apparatus

The LHD is one of the largest superconducting stellarator-type fusion devices with averaged major and minor radii of $R = 3.9$ m and $a = 0.6$ m, respectively [16]. The system includes three kinds of heating systems: ECH, NBI, and ion cyclotron heating.

In this paper, two external heating systems, ECH and NBIs are used. Plasmas are sustained by 3.8 MW ECH during each discharge. In this work, experiments were performed in a full-field standard magnetic configuration, $(B_t, R_{ax}) = (2.75$ T$, 3.6$ m$)$, where B_t and R_{ax} are the toroidal magnetic field strength on magnetic axis and the position of the magnetic axis with respect to the major radius, respectively. The direction of the toroidal magnetic field is counterclockwise. The
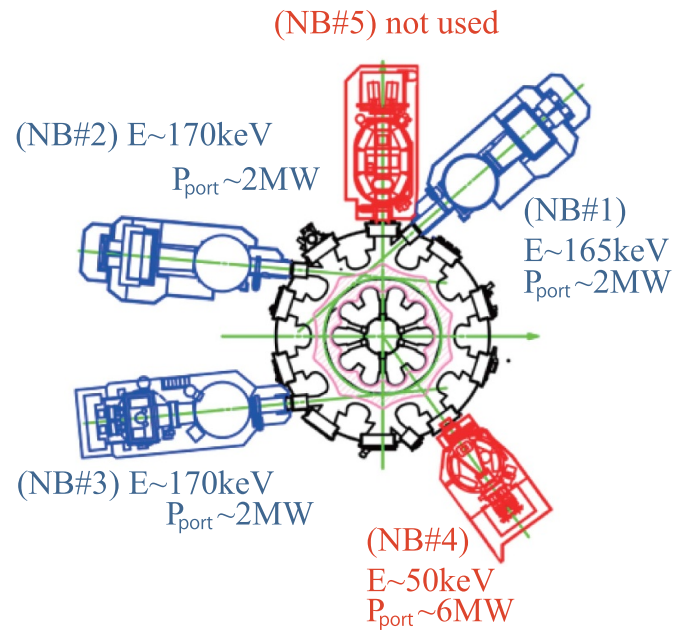
Figure 1. Top view of NBI system in the LHD. Typical beam injection energy and port-through power values are shown.

in-vessel cryo-sorption pump system installed near the divertor plate [17, 18] is used to control the neutral particles in the vacuum vessel.

The LHD is equipped with five NBs [19] as shown in figure 1. The typical injection energy and port-through power used in these experiments are also displayed. The three tangential NBs (NB#1-NB#3) are negative ion-based beams. The tangency major radius of NB#1 and NB#2 is $R = 3.7$ m and that of NB#3 is $R = 3.65$ m [20]. A positive ion-based perpendicular beam (NB#4) is used as a beam probe for the charge exchange spectroscopy (CXS) measurements. Because the direction of the toroidal magnetic field is counterclockwise, NB#1 and NB#3 have the co-direction to the magnetic field line.

The LHD includes several diagnostic systems [21]. The following measurements are used in this paper. The electron temperature T_e and density n_e profiles [22, 23] are determined based on the Thomson scattering diagnostics. The line-averaged electron density $\bar{n}_e$ is measured by a far infrared interferometer [24]. The ion temperature and carbon density n_C profiles are based on the CXS measurements obtained with the spectra of the CX line of carbon (C VI) using the neutral beam [25–27]. The time evolution of the neutron emission rate S_n is measured by a fast-response wide dynamic range neutron flux monitor [10].

2.2. Experimental scenario

Figure 2 shows the typical waveform used in these experiments. The plasma discharges start at $t = 3.3$ s with 3.8 MW ECH. The first beam, NB#1, is injected from $t = 3.3$ s to $t = 5.3$ s. The second beam, NB#3 (or NB#2), is injected at $t = 4.3$ s. In this paper, the period from $t = 3.3$ s to $t = 4.3$ s is called the 'single beam phase' and the period from $t = 4.3$ s
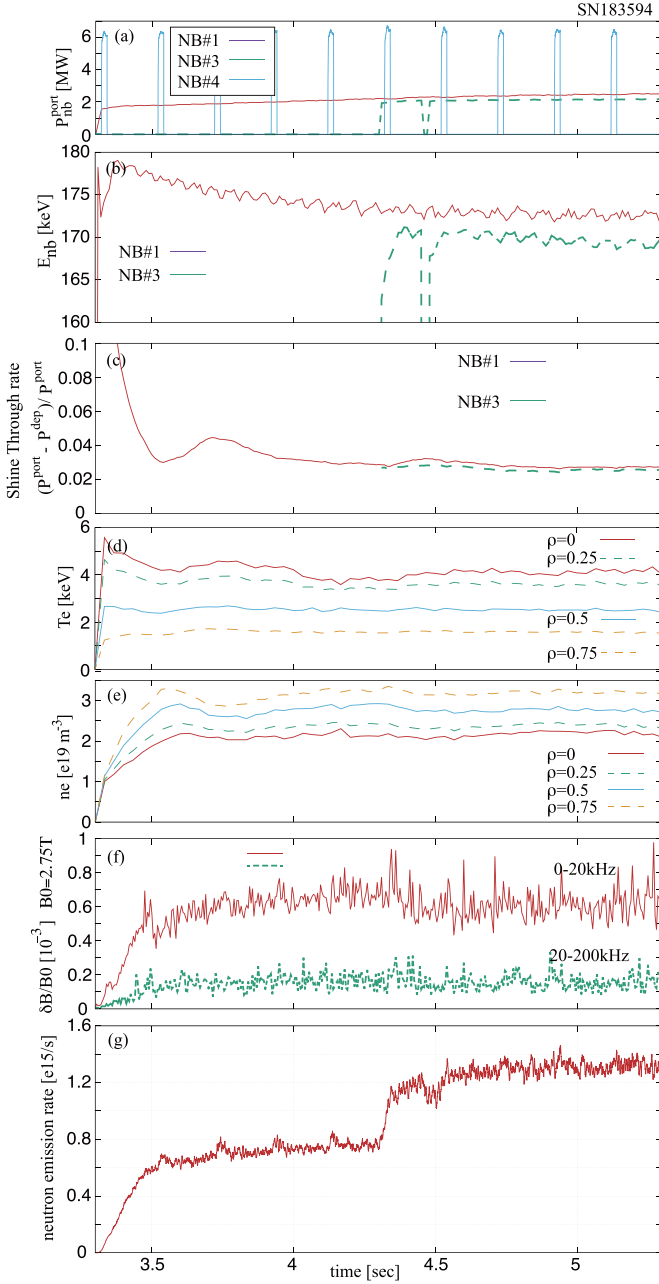
Figure 2. Typical waveform used in these experiments (shot number (SN) 183594). The figure shows (*a*) the NB port-through power and (*b*) injection energy in each beam, (*c*) the beam shine-through rate monitored by the calorimeter array on the armor tiles, (*d*) the electron temperature, (*e*) the electron density, (*f*) the magnetic fluctuation measured by the magnetic probe, and (*g*) the neutron emission rate.

to $t = 5.3$ s is called the 'double beam phase'. In addition, the case with NB#1 and NB#3 is called the 'co-injection case' and the case with NB#1 and NB#2 is called the 'balance injection case'. NB#4 is injected repeatedly with a 20 ms pulse in each 200 ms from $t = 3.32$ s.

We performed a density scan experiment from $\bar{n}_e \sim 0.75 \times 10^{19}$ m^{-3} to $\bar{n}_e \sim 4 \times 10^{19}$ m^{-3} for the co-injection case and

the balance injection case to evaluate the degradation of the fast-ion confinement. During a single discharge, there were no significant changes in T_e, n_e, the shine-through rate, or the magnetic fluctuation as shown in figure 2 except for immediately after the beginning of the discharge.

3. Experimental results

Figure 3 shows the degradation of the fast-ion confinement due to the increase in NB power. The *y*-axis value is S_n divided by the sum of the tangential NB port-through power times at the beam-thermal fusion cross-section and is normalized to that at $t = 4.2$ s. This can be expressed as follows:

$$g(t) = \frac{S_n}{\sum_{n=1}^{3} \langle \sigma v \rangle (E_{\text{inj},n}) P_n}, \tag{1}$$

$$y = g(t)/g(t = 4.2), \tag{2}$$

where subscript *n* indicates the number of tangential NBs, $\langle \sigma v \rangle_{nf}$ is the beam-thermal fusion reactivity [28, 29], $E_{\text{inj},n}$ is the NB injection energy, and P_n is the NB port-through power. This expression intends to show the neutron emission rate per injected beam power. The fusion cross-section is needed to correct the difference in the beam injection energies.

Figure 3 shows that the neutron emission rate per beam power decreases by up to 20% in the double beam phase than that in the single beam phase. According to our previous study [12, 15], the tangential NB fast-ions have approximately the same effective confinement time, $\tau_c^{\text{eff}} \sim 0.5$ s for each beam line. Using the same confinement time assumption in the case of each beam line, the simulated neutron emission rate per NB power is approximately the same for each beam line. Figure 4 shows the time evolution of the simulated neutron emission rate per NB power the same as figure 3. The details of the simulation method are provided in section 4 and appendix A. In figure 4, the reduction in the neutron emission rate per NB power does not appear after NB superpose. Therefore, the phenomena ignored in the simulation cause the reduction in the neutron emission rate per NB power.

The amplitude of the magnetic fluctuation measured by the magnetic probe does not change significantly due to the NB superpose as shown in figures 2(*e*) and 5. Because there are no significant variations in the electron temperature and density, the NB shine-through rate, or the magnetic fluctuation between the single beam phase and the double beam phase, the fast-ion confinement degradation appears to reduce the neutron emission rate per beam power.

Figure 6 shows a similar analysis to figure 3 for the balance injection case. The reduction in the neutron emission rate per beam power in the double beam phase also occurs for the relatively high-density ($\bar{n}_e > 2 \times 10^{19}$ m^{-3}) discharges. Because the number of fast-ions increases in the low-density discharges and the beam-beam fusion reaction is not negligible, the neutron emission rate per beam power in the double beam phase exceeds that in the single beam phase for $\bar{n}_e < 1.5 \times 10^{19}$ m^{-3}
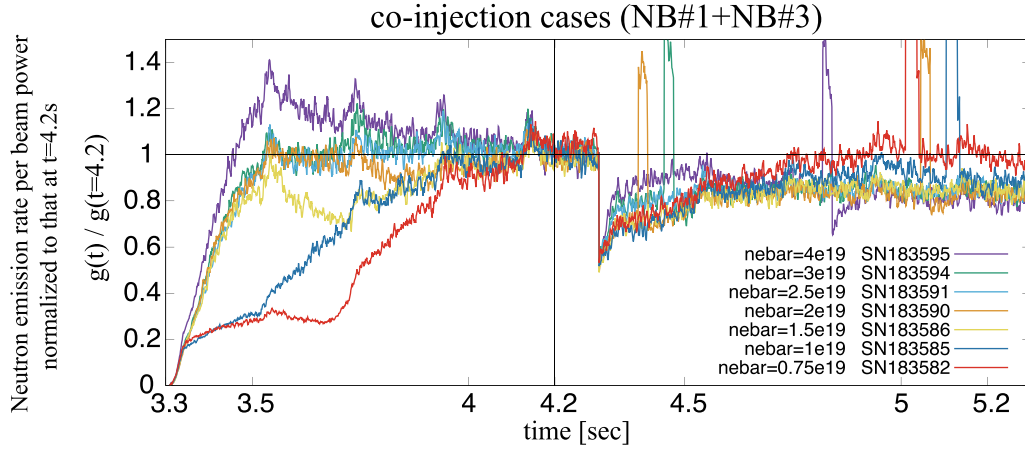
Figure 3. Time evolution of the neutron emission rate per beam power for the co-injection cases.
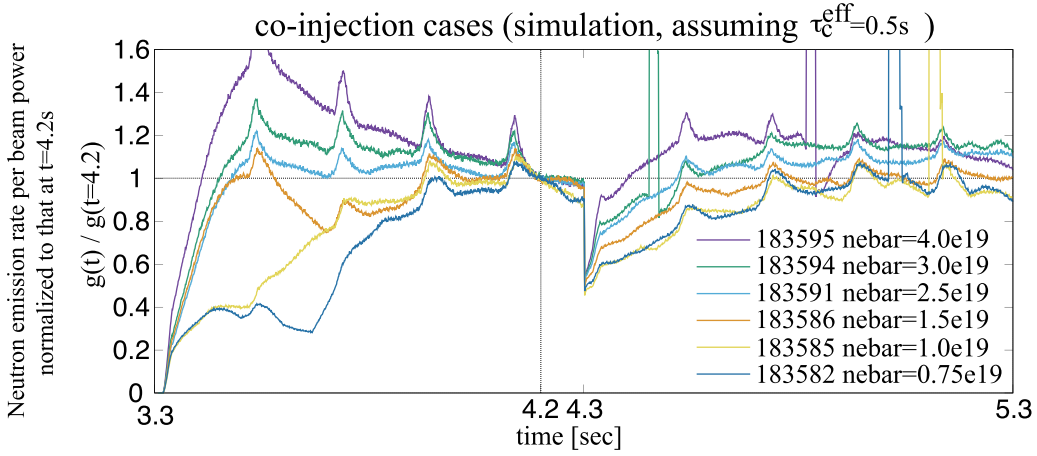
Figure 4. Time evolution of the simulated neutron emission rate per beam power for the co-injection cases.

discharges. Figure 7 shows the simulation results of the neutron emission rate per NB power assuming the constant effective confinement time $\tau_c^{\text{eff}} = 0.5$ s in the balance injection case. The reduction in the neutron emission rate per NB power for high-density discharges does not appear in the simulation result as the same as the co-injection case.

These results suggest that the fast-ion confinement degradation also occurs in the balance injection cases and that the degradation may not be noticeable due to the beam-beam fusion reaction in the low-density discharges. Figures 3 and 6 shows that the degradation of the fast-ion confinement depends on the beam power and does not depend on the beam direction.

3.1. Analysis model

To quantitatively estimate the degradation depending on the beam power, we formulate the following model. In our previous research [13, 15], the loss of the tangential NB fast-ions in the LHD was not dominated by the neo-classical transport but by another mechanism, which is probably the CX reaction due to the ambient neutrals. Here, the contribution of this CX loss is described by the time constant $\tau_{\text{cx}}^{\text{amb}}$. In addition, the neutron

decay time due to the fast-ion classic deceleration, which was originally used by Strachan *et al* [30], is expressed by τ_n^{cl}.

The time derivative of S_n can be expressed as

$$\frac{\partial S_n}{\partial t} = S - \frac{S_n}{\tau_n^{\text{cl}}} - \frac{S_n}{\tau_{\text{cx}}^{\text{amb}}} - \frac{P_{\text{NB}}^{\gamma} S_n}{\tau_{\text{ano}}}, \tag{3}$$

where S is the source term of the neutron emission rate due to the beam injection, P_{NB} is the dimensionless factor indicating the sum of the tangential NB port-through power normalized to 1 MW, γ is an arbitrary factor indicating the NB power dependence, and τ_{ano} is the time constant of the anomalous degradation per 1 MW beam power. The second and third terms on the RHS describe the decrease in the neutron emission rate due to the fast-ion deceleration and the CX loss with ambient neutrals. The fourth term is the anomalous fast-ion loss, which is the focus of this paper. By assuming uniform and steady-state plasma, the source term S can be roughly expressed as follows.

$$S \sim \int \mathrm{d}V n_D^{\text{bulk}} \langle \sigma v \rangle_{\text{nf}} (E_0) \left. \frac{\partial n_D^{\text{fast}}}{\partial t} \right|_{\text{birth}}$$
$$= C n_D^{\text{bulk}} P_{\text{NB}}, \tag{4}$$
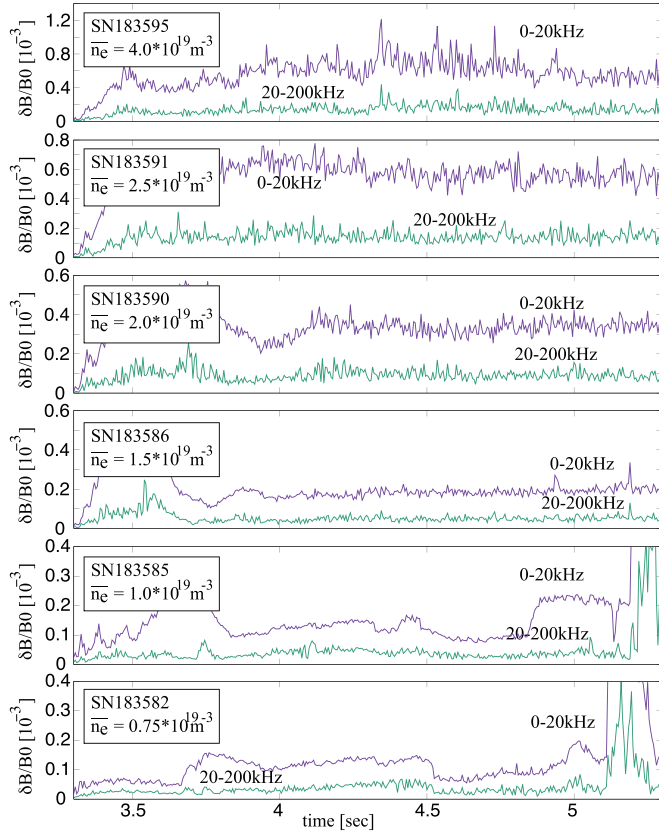
Figure 5. Time evolutions of $\delta B/B_0$ for each discharge in the co-injection case.

where n_D^{bulk} and n_D^{fast} are the bulk- and fast-deuteron densities, $<\sigma v>_{\text{nf}}(E_0)$ is the fusion reactivity for the beam energy E_0, E_0 is the beam injection energy, $\partial n_D^{\text{fast}}/\partial t|_{\text{birth}}$ is the fast-deuteron birth rate, and C is a constant factor related to the fusion cross-section and the beam ion birth rate. Because the beam injection energy, shine-through rate, plasma density, and temperature are constant in both phases, C can be viewed as a constant in a single discharge. For simplicity, n_D^{bulk} is written as n_D. τ_n^{cl} is formulated as

$$\tau_n^{\text{cl}} = \frac{\tau_{se}}{3} \ln\left(\frac{E_0^{3/2} + E_C^{3/2}}{E_1^{3/2} + E_C^{3/2}}\right), \tag{5}$$

$$\tau_{se} = \frac{3(2\pi)^{3/2}\epsilon_0^2 m_{\text{fast}} T_e^{3/2}}{n_e e^4 m_e^{1/2} \ln\Lambda}, \tag{6}$$

where τ_{se} is the Spitzer fast-ion slowing down time on electrons, E_1 is the beam energy satisfying the following relation:

$$\frac{\langle\sigma v\rangle_{nf}(E_1)}{\langle\sigma v\rangle_{nf}(E_0)} = 1/e. \tag{7}$$

The critical energy E_C is given by [15]

$$E_C^{3/2} = \frac{3\pi^{1/2}m_{\text{fast}}^{3/2}T_e^{3/2}}{4m_e^{1/2}}\left(\sum_i \frac{n_i Z_i^2}{n_e m_i}g(u_i)\right), \tag{8}$$

$$g(u_i) = \text{erf}(u_i) - u_i\text{erf}'(u_i), \tag{9}$$

$$\text{erf}(u) = \frac{2}{\pi}\int_0^u \exp\left(-x^2\right)dx \tag{10}$$

$$\text{erf}'(u) = \frac{2}{\pi}\exp\left(-u^2\right) \tag{11}$$

$$u_i = \frac{\sqrt{E_0/m_{\text{fast}}}}{v_{\text{th},i}}, \tag{12}$$

where erf is the error function, the subscript i indicates the ion species, and $v_{\text{th},i} = \sqrt{T_i/m_i}$ is the thermal velocity.

In the following, the values in the single beam phase and the double beam phase are represented by the subscripts s and d, respectively. Because the time derivative of S_n is 0 in the steady state, we can obtain the following expressions:

$$CP_{\text{NB},s}n_{D,s} = \left(\frac{1}{\tau_{n,s}^{\text{cl}}} + \frac{1}{\tau_{\text{cx}}^{\text{amb}}} + \frac{P_{\text{NB},s}^{\gamma}}{\tau_{\text{ano}}}\right)S_{n,s} \tag{13}$$

$$CP_{\text{NB},d}n_{D,d} = \left(\frac{1}{\tau_{n,d}^{\text{cl}}} + \frac{1}{\tau_{\text{cx}}^{\text{amb}}} + \frac{P_{\text{NB},d}^{\gamma}}{\tau_{\text{ano}}}\right)S_{n,d}. \tag{14}$$

Here, we introduce the fraction of the beam power and the neutron emission rate between the single and double beam phases as $P_{\text{NB},d}/P_{\text{NB},s} \equiv \alpha$ and $S_{n,d}/S_{n,s} \equiv \beta$, respectively. We can rewrite the expressions with the following relation:

$$\frac{\alpha}{n_{D,s}}\left(\frac{1}{\tau_{n,s}^{\text{cl}}} + \frac{1}{\tau_{\text{cx}}^{\text{amb}}} + \frac{P_{\text{NB},s}^{\gamma}}{\tau_{\text{ano}}}\right) = \frac{\beta}{n_{D,d}}\left(\frac{1}{\tau_{n,d}^{\text{cl}}} + \frac{1}{\tau_{\text{cx}}^{\text{amb}}} + \frac{P_{\text{NB},d}^{\gamma}}{\tau_{\text{ano}}}\right).$$

From this relation, we can obtain the expression for τ_{ano} as follows:

$$\tau_{\text{ano}} = \frac{\left(\frac{\beta}{n_{D,d}}P_{\text{NB,d}}^{\gamma} - \frac{\alpha}{n_{D,s}}P_{\text{NB,s}}^{\gamma}\right)\tau_{\text{cx}}^{\text{amb}}\tau_{n,s}^{\text{cl}}\tau_{n,d}^{\text{cl}}}{\frac{\alpha}{n_{D,s}}\tau_{n,s}^{\text{cl}}\tau_{n,d}^{\text{cl}} + \frac{\alpha}{n_{D,s}}\tau_{\text{cx}}^{\text{amb}}\tau_{n,d}^{\text{cl}} - \frac{\beta}{n_{D,d}}\tau_{n,s}^{\text{cl}}\tau_{n,d}^{\text{cl}} - \frac{\beta}{n_{D,d}}\tau_{\text{cx}}^{\text{amb}}\tau_{n,s}^{\text{cl}}}. \tag{15}$$

The effective confinement times in the single and double beam phases are given by

$$\left(\tau_{c,s}^{\text{eff}}\right)^{-1} = \left(\tau_{\text{cx}}^{\text{amb}}\right)^{-1} + \left(\frac{\tau_{\text{ano}}}{P_{\text{NB},s}^{\gamma}}\right)^{-1} \tag{16}$$

$$\left(\tau_{c,d}^{\text{eff}}\right)^{-1} = \left(\tau_{\text{cx}}^{\text{amb}}\right)^{-1} + \left(\frac{\tau_{\text{ano}}}{P_{\text{NB},d}^{\gamma}}\right)^{-1}. \tag{17}$$

Here, we choose the value $\tau_{\text{cx}}^{\text{amb}} = 0.55$ s based on the results of the short-pulse beam injection experiment [12, 13] and $\gamma = 1$ for simplicity.

In addition, we should choose the appropriate radial position for estimating plasma parameters such as T_e, n_e, T_i, and n_D. Figure 8 shows the radial profiles of the simulated neutron emission rate at $t = 5.2$ s for six discharges. The explanation of our simulation is provided in section 4. Figure 8 shows that the dominant position for the neutron emission is different in each discharge. Here, the position of the peak of the neutron emission rate profile is defined as $\rho = \rho_{\text{peak}}$ in each discharge. We estimate the time constants τ_{ano} and τ_c^{eff} using $\rho = \rho_{\text{peak}}$. The values in the single and double beam phases
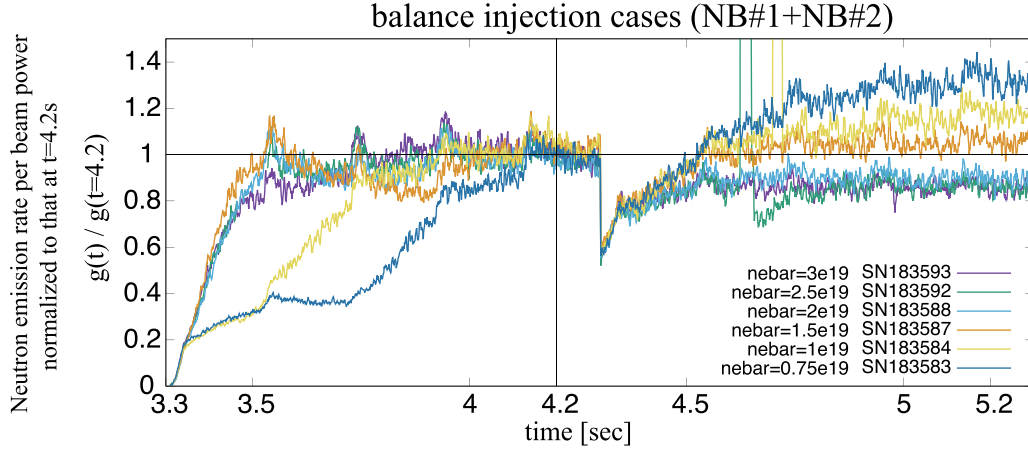
Figure 6. Time evolution of the neutron emission rate per beam power for the balance injection cases.
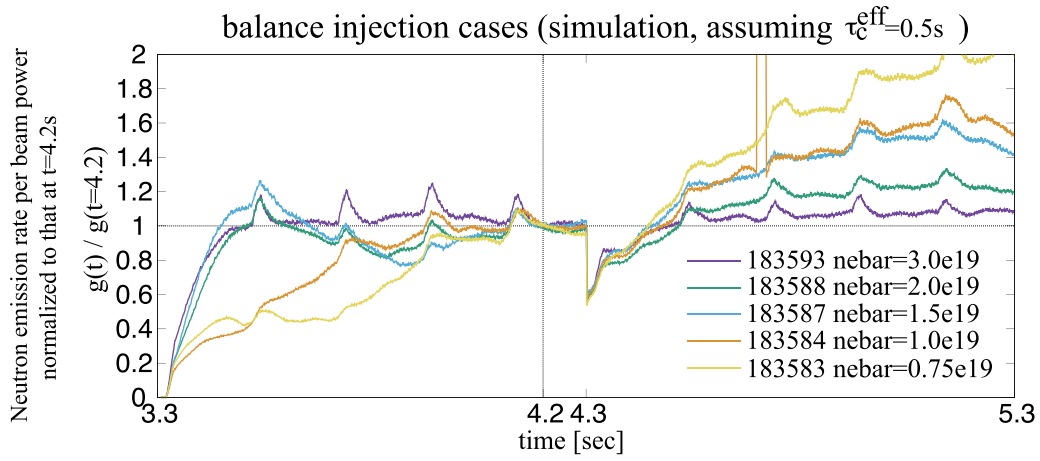
Figure 7. Time evolution of the simulated neutron emission rate per beam power for the balance injection cases.
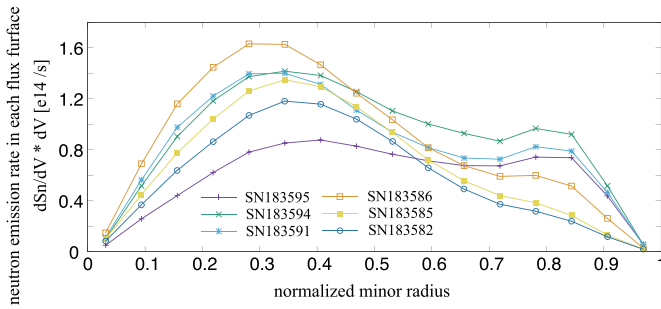
Figure 8. The simulation results of the radial profiles of the neutron emission rate at $t = 5.2$ s for six discharges in the co-injection case.

Table 1. The time constants of τ_{ano}, $\tau_{c,s}^{\mathrm{eff}}$, and $\tau_{c,d}^{\mathrm{eff}}$ with the electron density in the single phase at ρ_{peak} are shown.

SN	ρ_{peak}	$n_{e,s}$ (m^{-3})	τ_{ano} (s)	$\tau_{c,s}^{\mathrm{eff}}$ (s)	$\tau_{c,d}^{\mathrm{eff}}$ (s)
183 595	0.41	3.9×10^{19}	0.20	0.077	0.039
183 594	0.34	2.6×10^{19}	0.44	0.15	0.080
183 591	0.28	2.1×10^{19}	0.45	0.15	0.081
183 586	0.28	1.2×10^{19}	1.33	0.29	0.19
183 585	0.34	0.92×10^{19}	1.71	0.32	0.22
183 582	0.34	0.77×10^{19}	1.68	0.32	0.21

are given by the time average over 100 ms from $t = 4.2$ s and $t = 5.2$ s. The estimation method for n_D is provided in appendix A. For simplicity, $T_i = T_e$ is assumed. The results of time constants are shown in table 1. Because τ_{ano} is sensitive to n_e, the effective confinement time strongly depends on the electron density in contrast to the previous results in the short-pulse injection experiment [12, 13, 15]. In addition, the effective confinement time becomes sufficiently shorter than $\tau_{\mathrm{cx}}^{\mathrm{amb}}$.

4. Simulation results

4.1. Co-injection case

Here, the time evolution of the neutron emission rate is simulated using the obtained effective confinement times. The following simulations were performed by using TASK3D-a [14] and TASK/FP [31] codes. The fast-ion loss is described by the loss term, which is given by

$$\left. \frac{\partial f^1{}_D}{\partial t} \right|_{\mathrm{loss}} = -\frac{f_D^1}{\tau_c^{\mathrm{eff}}}, \tag{18}$$

where f_D^1 is the velocity distribution function of the fast-deuteron. A detailed description of the simulation method is provided in appendix A. Although the fast-ion loss and degradation should have velocity and spatial dependency, this simulation does not consider these dependencies on $\tau_c^{\rm eff}$.

By using the effective confinement times shown in table 1, the neutron emission rate simulation is simulated, as shown in figure 9. The simulation results are in good agreement with the measurements for the six discharges. Therefore, the effective confinement times listed in table 1 are valid.

Figure 10 shows the $n_e(\rho_{\rm peak})$ dependence of the anomalous diffusion coefficient $D_{\rm ano}$. The relation between $\tau_{\rm ano}$ and $D_{\rm ano}$ is given by $D_{\rm ano} = a^2/(5.8\tau_{\rm ano})$ [32], where a is the plasma minor radius. Here, we use $a = 0.6$ m for simplicity. Figure 10 shows that the anomalous degradation has an approximately linear dependency on $n_e(\rho_{\rm peak})$ except for the highest density discharge. Although the actual dependency may not be linear, the linear fitting is chosen for simplicity because the degradation mechanism is still unclear. The fitting aims not to clarify the degradation mechanism but to apply the degradation to the balance injection case in the following section. According to the weighted least-mean-square fitting approach, the relation between $D_{\rm ano}$ and $n_e(\rho_{\rm peak})$ is given by

$$D_{\rm ano} = (0.049 \pm 0.005) \times n_e(\rho_{\rm peak}) \times 10^{-19}, \qquad (19)$$

where $n_e(\rho)$ is in m^{-3}.

4.2. Balance injection case

Equation (15) can not be applied for the balance injection case because the beam-beam fusion reaction is not negligible. Due to the beam-beam fusion, the assumption that the factor C in equation (4) is constant between in the single and double beam phases is violated. Therefore, we estimate the effective confinement time $\tau_c^{\rm eff}$ for the balance injection cases based on the fitting line of $\tau_{\rm ano}$, as shown in equation (19).

Figure 11 shows the simulation results of the neutron emission rate considering the effective confinement times for five discharges in the balance injection cases. We note that the discharge with $\bar{n}_e = 2.5 \times 10^{19}\,{\rm m}^{-3}$ (SN183592), which is shown in figure 6, is omitted in figure 11 because the n_e and T_e measurements are poor for this discharge. Figure 11 demonstrates that the simulations considering the effective confinement times show good agreement for all discharges, even in the balance injection cases. Based on this result, equation (19) can be used to evaluate the anomalous degradation of the fast-ion confinement with sufficient accuracy. In addition, the model shown in equation (15) can describe the degradation in this range of the plasma parameters and for this magnetic configuration.

5. Discussion

5.1. NB heating efficiency

Our previous research [12, 13, 15] showed that the confinement time of the tangential NB fast-ions is not sensitive to the
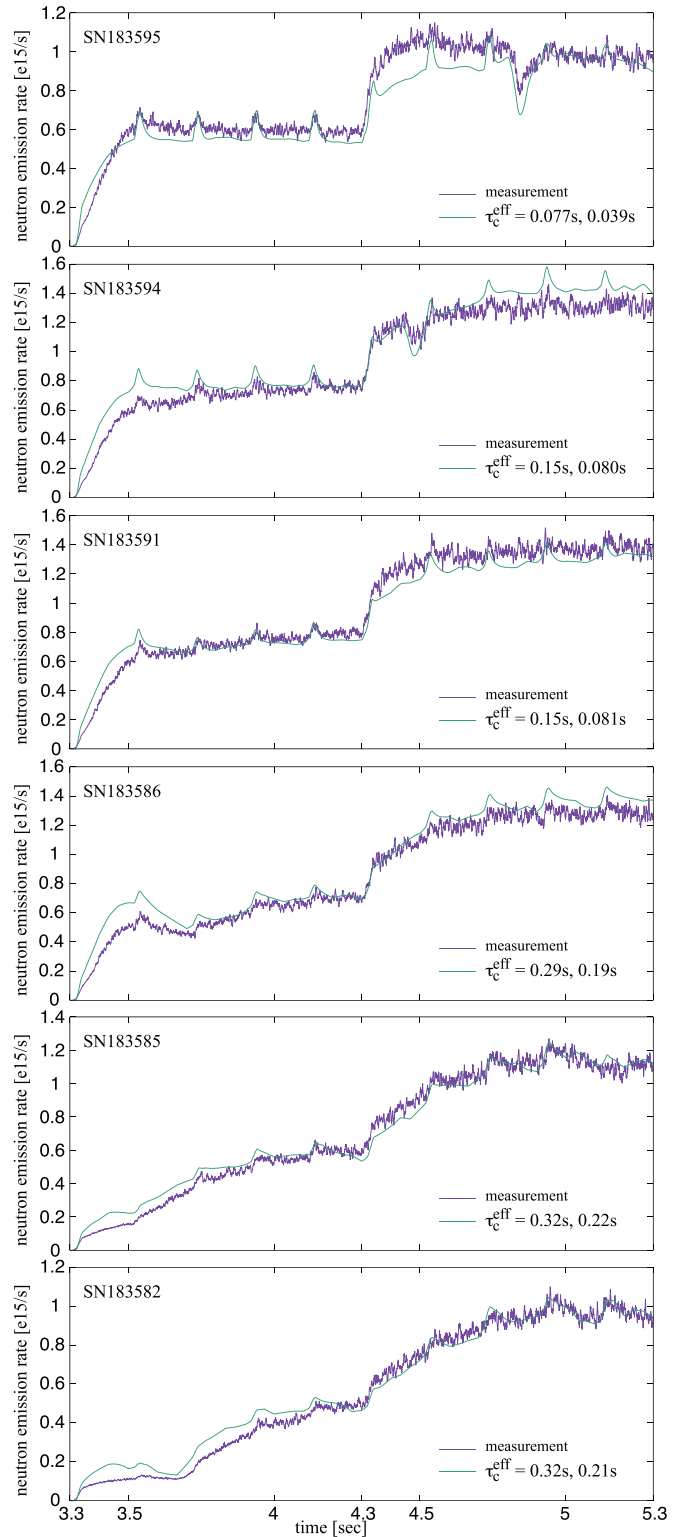
Figure 9. Time evolutions of the neutron emission rate for $0.75 \times 10^{19}\,{\rm m}^{-3} < \bar{n}_e < 4 \times 10^{19}\,{\rm m}^{-3}$ with the effective confinement times listed in table 1.

plasma density in short-pulse NB injection experiments. This means that the tangential NB heating efficiency increased with increasing plasma density because the fast-ion slowing down time decreases with increasing plasma density. However, as
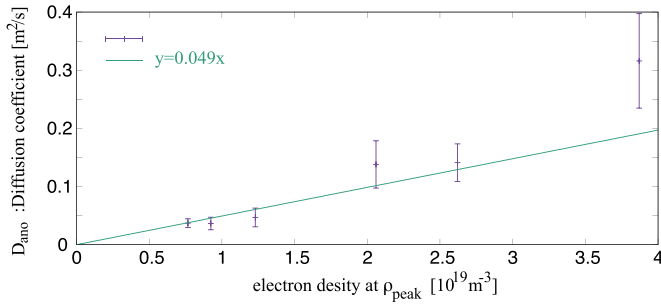
Figure 10. The diffusion coefficient of the anomalous fast-ion loss with $n_e(\rho_{peak})$ is shown. The *y*-axis error bar is estimated from the standard deviations of n_e, T_e, and n_C and the statistical error of the neutron count.

shown in figure 10, the fast-ion confinement degrades with increasing plasma density in typical NB heating discharges. Therefore, the efficiency of the NB heating should be investigated.

Figure 12 shows the fraction between the effective confinement time $\tau_{c,s}^{eff}$ and the fast-ion energy dissipation time due to the classical deceleration $\tau_{se,s}/2$ with $n_{e,s}(\rho_{peak})$. If the confinement degradation is not considered ($D_{ano} = 0$ and $\tau_c^{eff} = \tau_{cx}^{amb} = 0.55$ s), the fraction exceeds unity with $n_{e,s}(\rho_{peak}) > 2 \times 10^{19}$ m^{-3} as shown in the green curve. However, with the actual effective confinement time obtained in this paper, the fraction remains less than unity in the whole density range as shown in the red curve. This means that the fast-ion confinement degradation obtained in this paper makes the NB heating efficiency poor in the whole density range.

Figure 13 shows the NB heating simulation results with TASK/FP in SN183594 discharge. Because of the confinement degradation, the NB heating power per NB port-through power is less than 0.5 at $t = 5.3$ s as shown in red and green curves.

5.2. Investigation of the degradation mechanism

Although we quantitatively estimated the actual fast-ion confinement time in LHD deuterium plasmas with deuterium beams, the discussions provided in the previous sections do not clarify the confinement degradation mechanism. Therefore, it is unclear whether this degradation occurs in other cases, such as different species of plasmas, different magnetic configurations, and different beam ion species. Therefore, the anomalous degradation mechanism discussed in this paper must be clarified to applying this loss to other cases. In this section, we investigate the features of the fast-ion loss and the plausible candidates of the loss mechanism.

5.2.1. NB power dependence.
Until here, we assumed that the degradation is proportional to the NB power, $\gamma = 1$ in equation (3). Because the degradation mechanism is still not clarified, the assumption of linear dependence has no theoretical evidence. Therefore, we should discuss the plausible dependency.

Figure 14(*a*) shows the dependency of the effective confinement time on γ. Because the effective confinement time
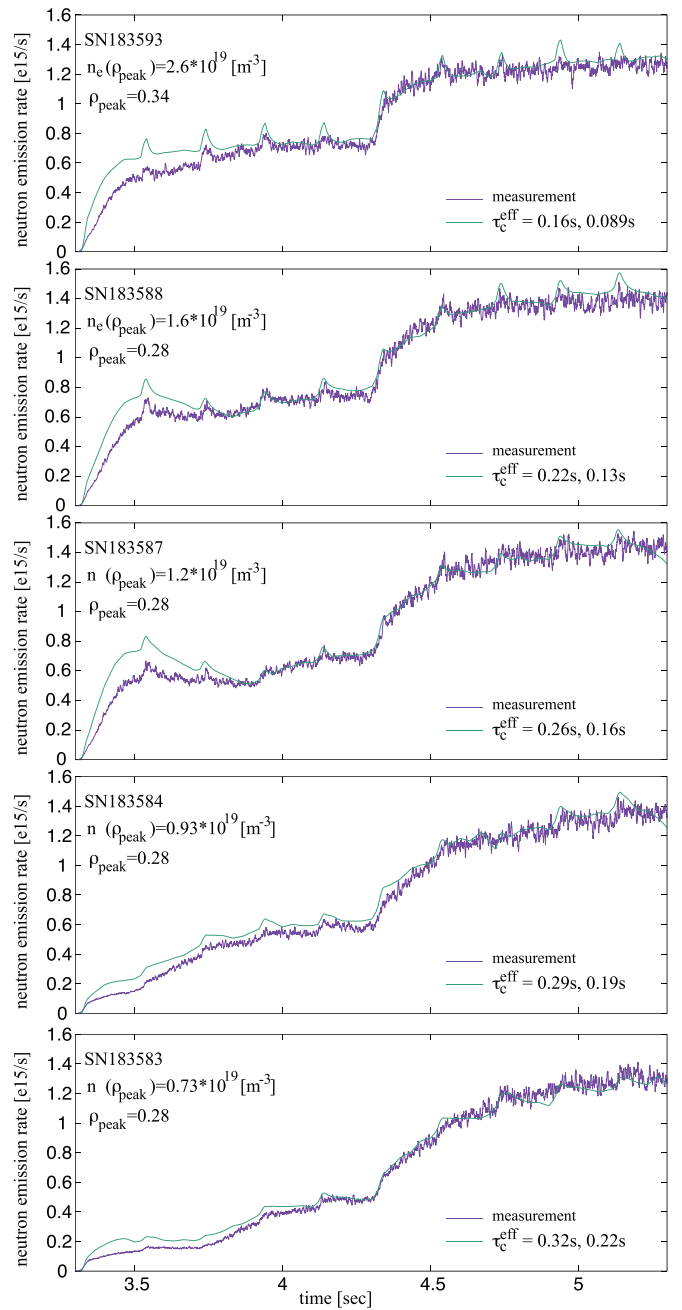
Figure 11. The measured and simulated neutron emission rates for the balance injection cases with the effective confinement times estimated by equation (19).

is sensitive to γ, the neutron emission rate simulations with $\gamma = 0.5$ and $\gamma = 1.5$ can not reproduce the measurement as shown in figure 14(*b*). For this result, the assumption of linear dependency is plausible.

5.2.2. Radial and velocity dependence of the degradation.
As noted in section 4, simulations in the previous section ignore the spatial and velocity dependence on the fast-ion loss term because the loss and degradation mechanisms are not clarified. Here, we discuss the spatial and velocity dependences on the degradation using fast-ion measurements.
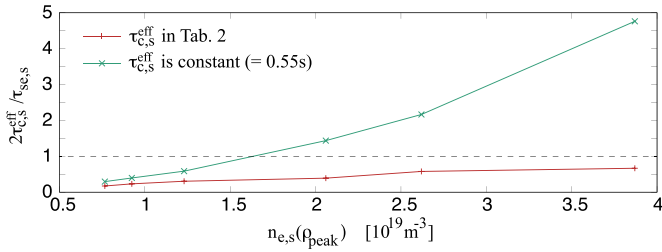
Figure 12. The fraction between the effective confinement time τ_c^{eff} and the fast-ion energy dissipation time due to the deceleration $\tau_{se}/2$ in the single beam phase with $n_{e,s}(\rho_{\text{peak}})$ is shown. The effective confinement time used for the red curve is presented in table 1 and the effective confinement time used for the green curve is $\tau_{c,s}^{\text{eff}} = 0.55$ s.
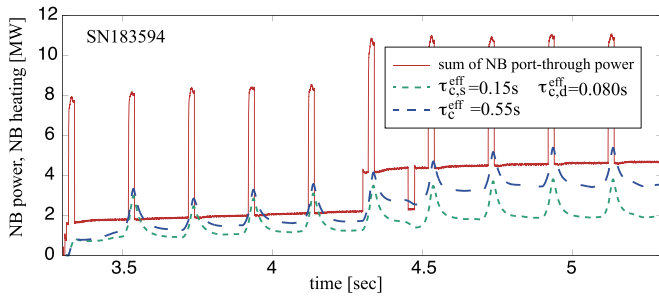
Figure 13. The time evolutions of the NB port-through power and the NB heating are shown (SN183594). The red-solid and green-dotted curves indicate the sum of the NB port-through power and the simulation results of the NB heating power to the plasma with $\tau_{c,s}^{\text{eff}} = 0.15$ s and $\tau_{c,d}^{\text{eff}} = 0.080$ s. The blue-dashed curve is the simulation result with $\tau_c^{\text{eff}} = 0.55$ s intending the no confinement degradation.
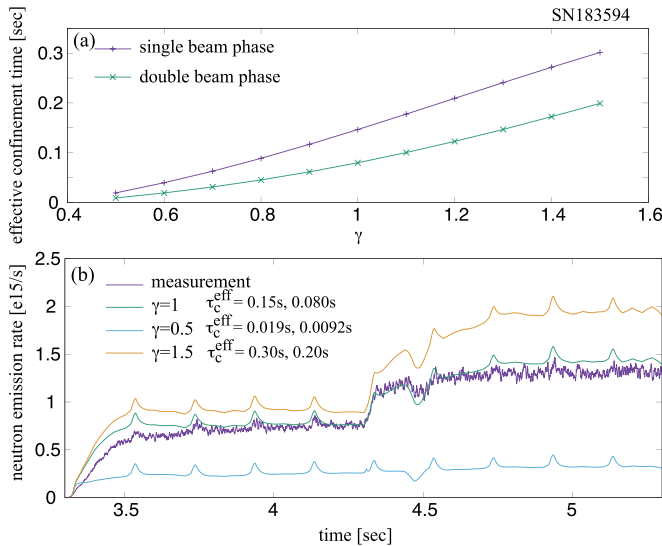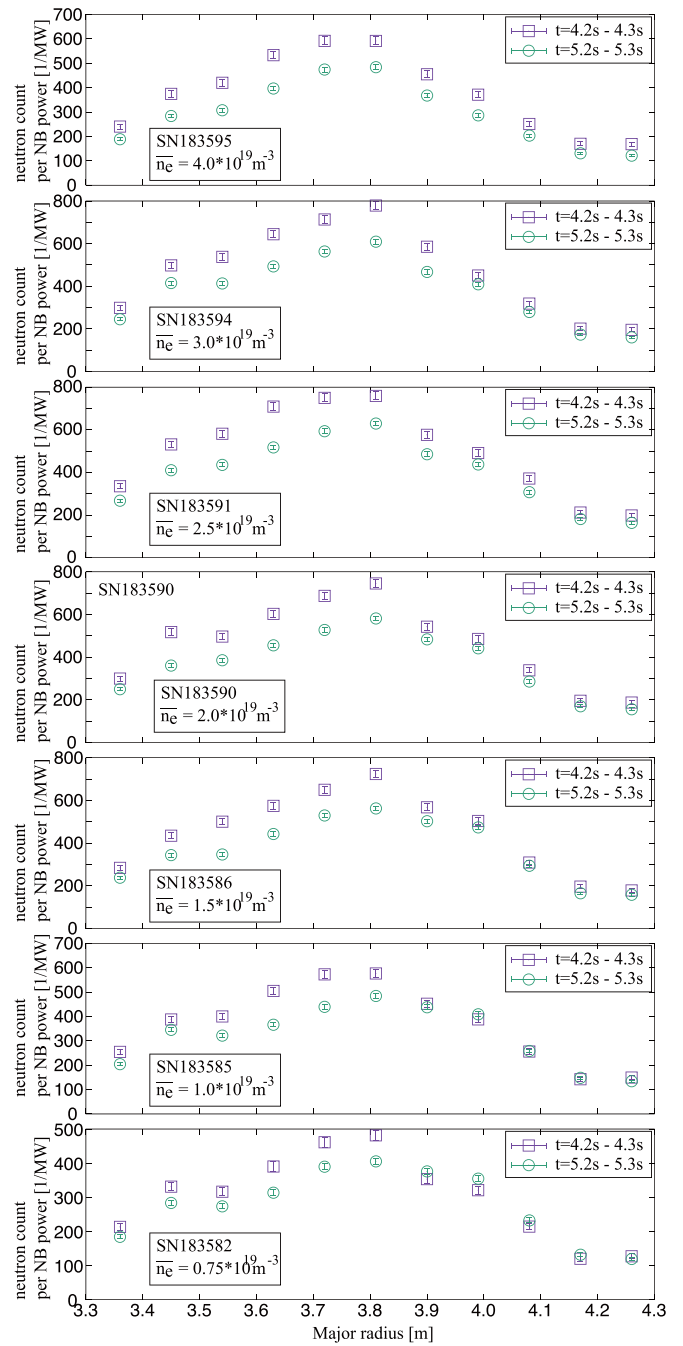

Figure 14. (*a*) The dependency of the effective confinement time on γ is shown for the high-density co-injection discharge (SN183594). (*b*) The neutron emission rate simulations with $\gamma = 0.5$ and $\gamma = 1.5$ are shown.

In the LHD, the vertical neutron camera (VNC) has been installed [33] to measure the radial profile of the neutron emission rate. Figures 15 and 16 show the neutron count per NB

Figure 15. Neutron count per NB power against the major radius in the co-injection cases are shown.

power against the major radius in the co-injection and the balance injection cases. The neutron count is cumulated over 100 ms from $t = 4.2$ s (single beam phase) or $t = 5.2$ s (double beam phase). Note that the sight lines of the VNC measurement are placed on the vertically elongated cross-section. Although the effective plasma minor radius is approximately $r_{\text{eff}} = 0.6$ m and the magnetic axis is $R_{\text{ax}} = 3.6$ m, the plasma boundary is inner than $R = 4.2$ m. Therefore, the sight line at $R = 4.26$ m is out of the plasma boundary. The values at $R = 4.26$ m indicate the background neutron count from the outer of the sight line.

Figure 16. Neutron count per NB power against the major radius in the balance injection cases are shown.

Figure 17. Measured spectra of FIDA measurement divided by NB power at $t = 4.13$ s and $t = 5.13$ s are shown for (*a*) the co-injection case (SN183585) and (*b*) the balance injection case (SN183584). The signal is cumulated over $\rho < 0.33$ region.

degradation is not uniform and dominant around the magnetic axis.

Fast-Ion D Alpha (FIDA) measurement [35] installed in LHD [36] can estimate the fast-ion velocity distribution. FIDA measurement is available only in low-density discharges ($\bar{n}_e \lesssim 1 \times 10^{19}$ m^{-3}) because FIDA signal intensity is not enough in high-density discharges to estimate the velocity distribution. Because the confinement degradation is remarkable in high-density discharges, it might be difficult to observe the velocity dependence of the confinement degradation using FIDA.

Figure 17(*a*) shows the spectra of FIDA measurement in the co-injection case in the low-density discharge (SN183585, $\bar{n}_e = 1 \times 10^{19}$ m^{-3}). The *x*-axis indicates the wavelength and the *y*-axis indicates the intensity of light normalized to the sum of NB power (NB#1 and NB#3) at each time. In the $\lambda < \sim 659$ nm region, non-FIDA emission components are dominant. In contrast, in the $\lambda > \sim 659$ nm region, FIDA emission is dominant. In figure 17(*a*), the reduction of the FIDA signal per NB power appears in the high-energy region (longer wavelength region). As noted above, however, it is not clear whether the cause of the reduction is the degradation or other mechanisms such as the difference in the tangency major radius of NB#1 and NB#3.

Figure 17(*b*) shows the spectra of FIDA measurement in the balance injection case in the low-density discharge (SN183584, $\bar{n}_e = 1 \times 10^{19}$ m^{-3}). In figure 17(*b*), the values of the *y*-axis are normalized to the NB#1 power because the two beam directions are opposite each other and the FIDA signal from NB#1 and NB#2 are separated in the wavelength (the FIDA signal of NB#2 appears in $\lambda < 654$ nm). Figure 17(*b*) shows the FIDA component of NB#1 per NB power slightly decreases after NB#2 superpose. However, it is difficult to estimate the energy dependence. Although the detailed discussions require the five-dimensional orbit simulation and FIDASIM [37, 38], they are left for future work.

The reduction of the neutron count per NB power after NB superpose is also observed in the VNC measurement. The reduction mainly appears around the magnetic axis ($3.45 < R < 3.81$) rather than the peripheral region in the co-injection case. Similarly, the reduction appears in the balance injection case for high-density discharges. However, it is noted that the decrement of the profile of the neutron count per NB power is not necessarily the confinement degradation. This is because the neutron emission profile of the co-direction beam (NB#1) is different from that of the counter-direction beam (NB#2) due to the finite orbit effect [34]. Similarly, the neutron emission profile of NB#1 is not necessarily the same as that of NB#3 because the tangency major radius of NB#1 and NB#3 is slightly different. Although the strict estimation of the radial profile of the confinement degradation requires a comparison to the orbit simulation, at least, figures 15 and 16 show that the
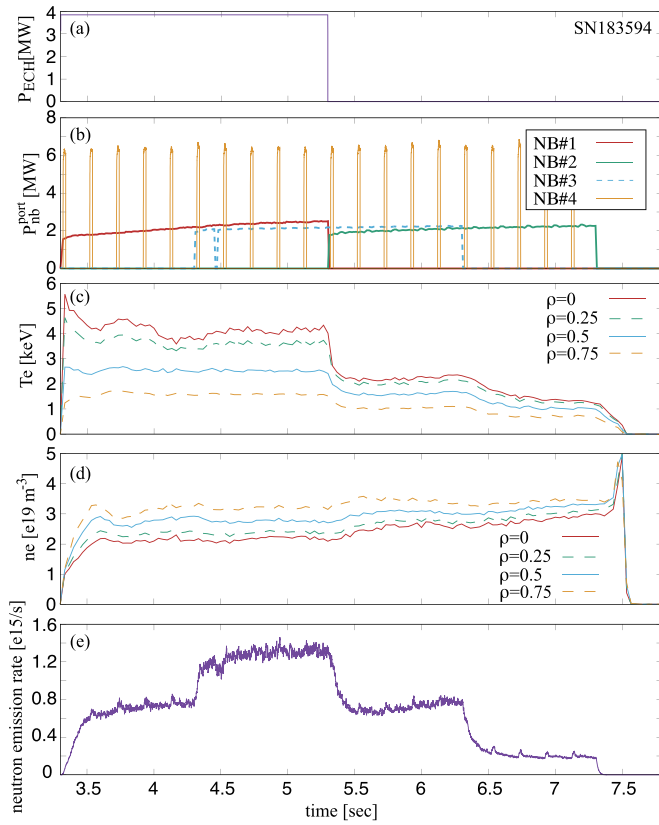
Figure 18. Typical waveform used in these experiments (shot number (SN) 183 594) including after $t = 5.3$ s. The figure shows (*a*) the power of ECH heating, (*b*) the NB port-through power in each beam, (*c*) the electron temperature, (*d*) the electron density, and (*f*) the neutron emission rate.

5.2.3. Extension of the focus region.

From here, we extend the focus region from 3.3 s $< t < 5.3$ s to 3.3 s $< t < 7.8$ s to investigate the degradation mechanism. The typical waveform including after $t = 5.3$ s is shown in figure 18. Because the ECH heating is turned off at $t = 5.3$ s, the plasma parameters are changed rapidly after $t = 5.3$ s. Although NB#1 is also turned off at $t = 5.3$ s, the rest of the tangential NB (NB#2 or NB#3) is injected from the time. Therefore, injected NB power is kept at ~ 4 MW until $t = 6.3$ s. In contrast, the neutron emission rate is dropped at $t = 5.3$ s due to the sharp drop in the electron temperature.

We estimate the effective confinement time τ_c^{eff} after $t = 5.3$ s based on the fitting line of τ_{ano}, as shown in equation (19). We investigate the validity of the obtained confinement time after $t = 5.3$ s through the neutron emission rate simulation. Figure 19 shows the time evolutions of the measured and simulated neutron emission rate including after ECH turned off. The purple and green curves indicate the neutron emission rate for the 'co-injection' and the 'balance injection' cases The red-dotted and black-dashed curves indicate the simulation results. The values of the effective confinement times are shown in each figure. Note that the highest density discharge (SN183595, $\bar{n}_e \sim 4 \times 10^{19}$ m^{-3}) is omitted here because the same density discharge in the balance injection case is lacked and the D_{ano} value is separated from the fitting line slightly.
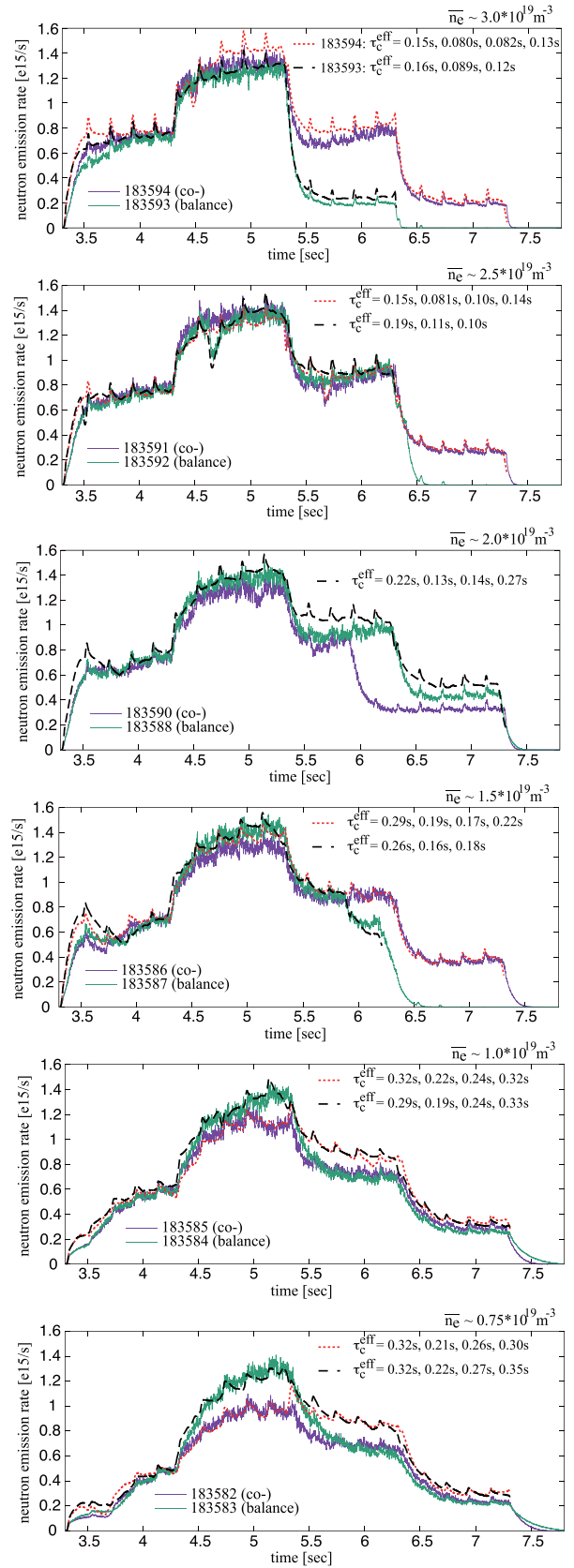
Figure 19. Time evolutions of the measured and simulated neutron emission rate for co-injection and balance injection cases. In some balance injection discharges, NB#3 is broken down after $t = 5.3$ s. The simulation is ended at the time that all heating is ended to avoid abnormal termination.
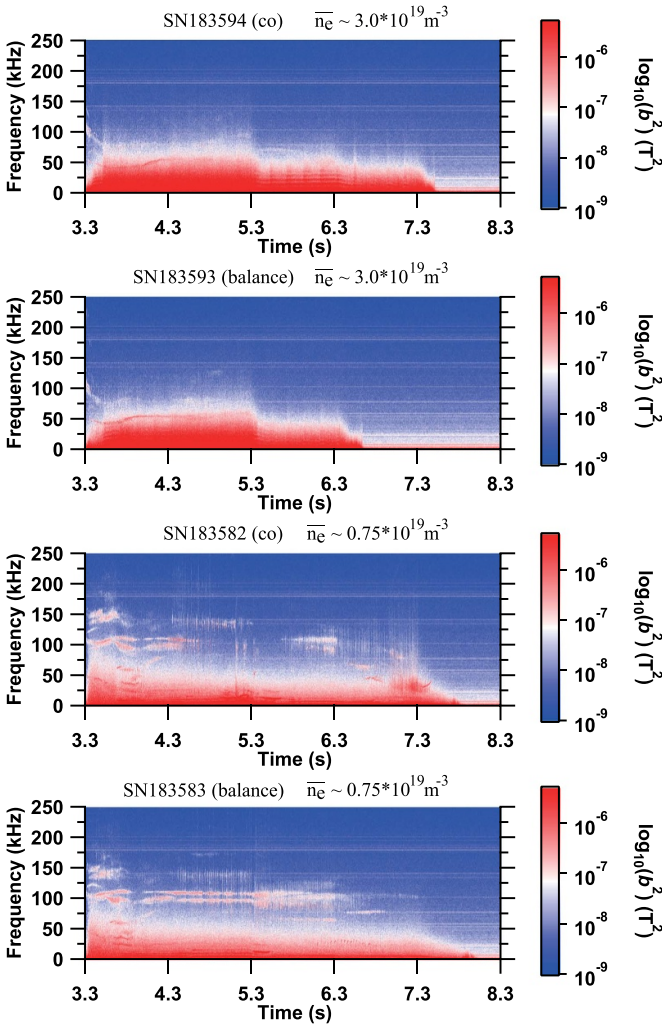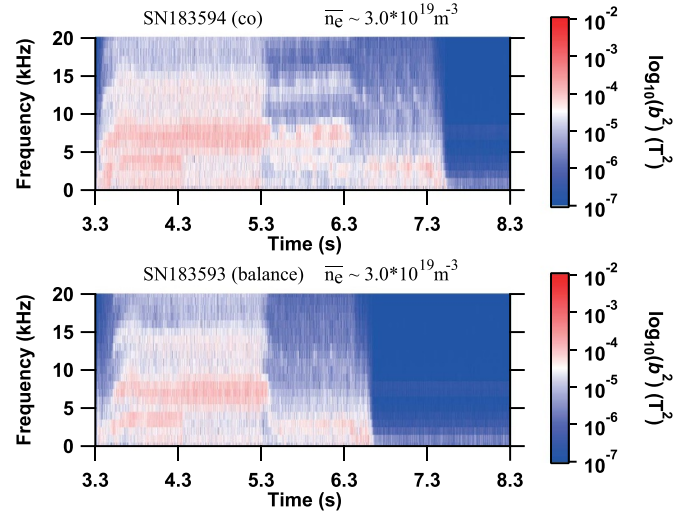
Figure 20. The spectrograms of the magnetic activity for high-density discharges ($\bar{n}_e \sim 3 \times 10^{19}$ m^{-3}) and low-density discharges ($\bar{n}_e \sim 0.75 \times 10^{19}$ m^{-3}) are shown.

Although slightly overestimated, the simulation results are in good agreement even after $t = 5.3$ s for $\bar{n}_e > 1 \times 10^{19}$ m^{-3} discharges except for SN183588. In contrast, for $\bar{n}_e \leqq 1 \times 10^{19}$ m^{-3} discharges, the simulation results are in poor agreement after $t = 5.3$ s due to overestimation. The overestimation of the simulation result indicates the further degradation of the fast-ion confinement. For these results, the confinement degradation also occurs after ECH is turned off.

5.2.4. Candidates can be excluded. It is well known that the energetic-particle (EP) driven instabilities cause the fast-ion loss which depends on NB power. Therefore, at first, we investigate the high frequency ($\sim$100 kHz) EP-driven instabilities. Figure 20 shows the spectrograms of the magnetic activity for high-density and low-density cases. The high frequency ($\sim$100 kHz) modes are observed continuously only in low-density balance injection discharge (SN183583). Although the high-frequency activity is different in two low-density discharges, the neutron emission rate simulation is in good agreement before $t < 5.3$ s for both cases as shown in figure 19.

Figure 21. The spectrograms of the low-frequency magnetic activity for high-density discharges ($\bar{n}_e \sim 3 \times 10^{19}$ m^{-3}) are shown.

For this reason, EP-driven instability does not play an important role in the fast-ion confinement degradation in these discharges. In addition, EP-driven instabilities can not explain the higher loss in high-density discharges. Therefore, the EP-driven instabilities can be excluded from the candidates.

In contrast, as shown in figure 5, the amplitude of low-frequency ($\lesssim$20 kHz) magnetic perturbation increases with increasing plasma density. In general, the higher plasma pressure can drive low-frequency modes, such as the interchange mode. This trend is consistent with the degradation dependence on the electron density. In addition, the change of beam-driven current deforms the profile of the rotational transform, ι. Because MHD instabilities are sensitive to the ι profile, there is a possibility that the changing of NB power causes low-frequency MHD instabilities through the changing of the ι profile. Therefore, the contribution of low-frequency modes to the fast-ion loss should be discussed.

Figure 21 shows the spectrograms of low-frequency ($<$20 kHz) magnetic activity for high-density discharges. The amplitude of low-frequency modes has no significant increase after NB superpose. In addition, the amplitude decreases clearly after ECH is turned off in both cases. Despite of the change of low-frequency activity, the fast-ion confinement degradation continues after ECH is turned off as shown in figure 19. For these reasons, low-frequency modes do not contribute to the confinement degradation. Therefore, the low-frequency instabilities also can be excluded from the candidates.

There are other mechanisms, which can cause the fast-ion loss depending on NB power. Non-linear Coulomb collision effect and beam-particle self-interaction (BPSI) are some of them. Because non-linear Coulomb collision between fast-ions can enhance the pitch angle scattering, much radial particle flux is induced due to the neo-classical transport [39]. It is known that the BPSI effect, which is based on the charge exchange loss between beam neutrals and fast-ions, can enhance the beam-stopping cross-section [40]. This effect also
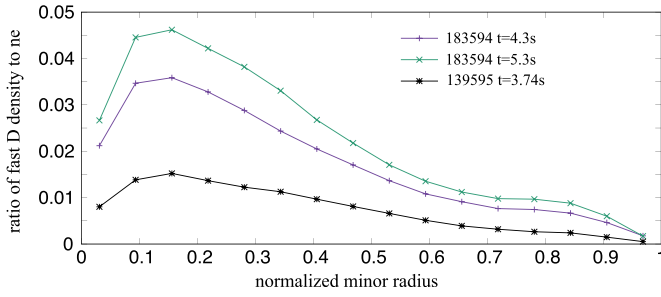
Figure 22. Radial profiles of the ratio of the fast-deuteron density to the electron density, n_D^1/n_e are shown for the high-density steady-state case (SN183594) and the low-density short-pulse case (SN139595). The simulation results for steady-state include the confinement degradation. In contrast, the simulation for short-pulse experiment assumes $\tau_c^{\mathrm{eff}} = 0.5$ s.

leads the fast-ion loss. However, these effects can be excluded from the confinement degradation mechanisms for two reasons. One is that these effects can contribute only to the co-injection case because the low relative velocity is required for two reactant particles (between fast-ions or a beam neutral and a fast-ion). Another is that these effects become significant for low-density discharges.

The neutral beam current drive can deform the MHD equilibrium. The change in the magnetic configuration can affect the pitch angle of NB fast-ions and the radial particle flux. However, this effect also depends on the superposed beam direction and becomes important for low-density discharges. This conflicts with the features of the observed degradation. Therefore, this is also excluded.

5.2.5. Difference to the short-pulse injection experiment. The confinement degradation with increasing plasma density was not observed in the previous short-pulse NB injection experiment [12, 13, 15]. Therefore, we should discuss the difference between the two series of experiments.

The most clear difference is the fast-ion population due to the difference in the pulse duration. Figure 22 shows the radial profiles of the fast-deuteron density ratio to the electron density for the high-density steady-state case (SN183594, $\tau_n^{\mathrm{cl}} \sim 0.16$) and the low-density short-pulse case (SN139595, $\tau_n^{\mathrm{cl}} \sim 0.22$). In the short-pulse experiment, the ratio of the fast-ion is up to $\sim 1.5\%$ at the peak position. In contrast, in the steady-state, the ratio is at least $\sim 3.5\%$ in the single beam phase. In the low-density discharge (SN183582), the ratio reaches up to $\sim 40\%$ in the double beam phase.

Differences in the heating pattern may affect the impurity profile. Figures 23 and 24 show the time evolutions of Z_{eff} at three radial positions. Although the mechanism of impurity transport is a big issue and still unclear, it is found that the Z_{eff} trend changes at the heating pattern switching timing from figures 23 and 24 (see $t = 4.3$ s and 5.3 s). In contrast, only NB turned on and off is the heating pattern switching in the short-pulse NB injection experiments. For this reason, Z_{eff} profile may be kept constant in time though n_C was not measured.
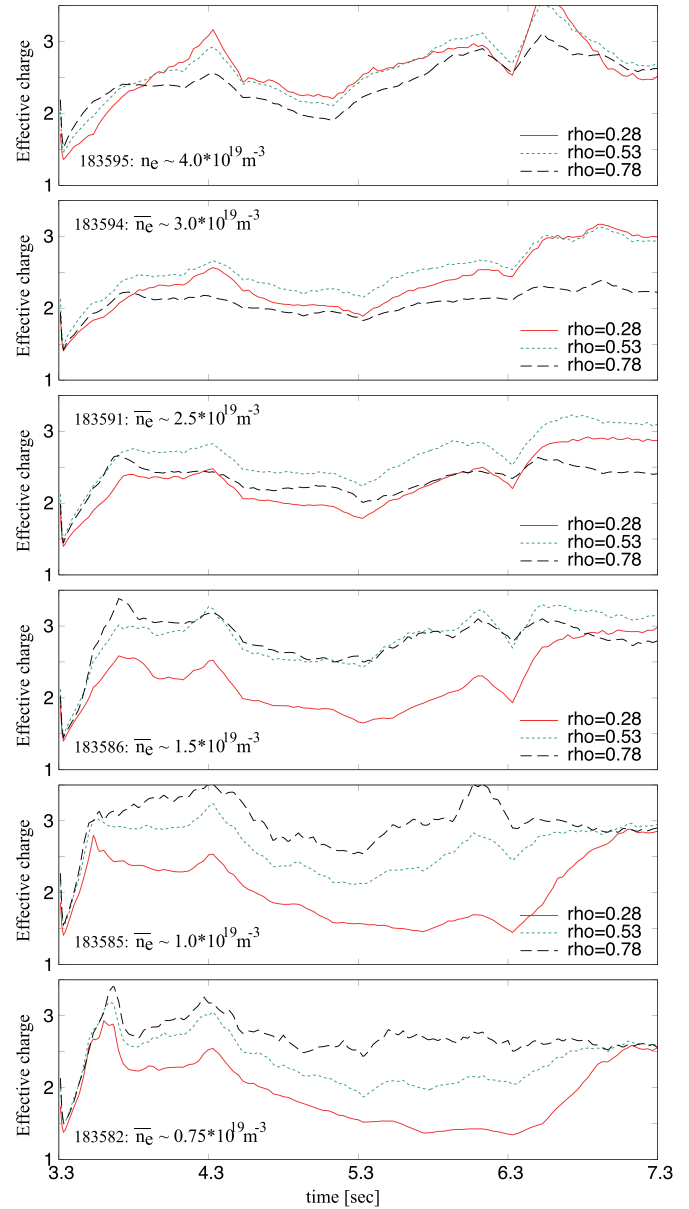
Figure 23. Time evolutions of Z_{eff} at $\rho = 0.28$, 0.53, and 0.78 in the co-injection cases.

The differences in the fast-ion population and the impurity profile may affect the radial electric field. The fast-ion confinement may be changed through the change of the radial electric field [41, 42]. The difference in the fast-ion population affects to the pressure anisotropy and the plasma flow. The role of them to the fast-ion confinement also should be investigate.

We have another viewpoint on the differences between these experiments. In the short-pulse NB injection experiments, we investigated the neutron decay time after NBs were turned off to estimate τ_c^{eff}. There are two reasons that we did not focus on the beam-injected phase (neutron-increasing phase). One is that the neutron decay time is not sensitive to uncertain values such as Z_{eff}. Another is that estimating τ_c^{eff} is difficult in the beam-injected phase because dS_n/dt is
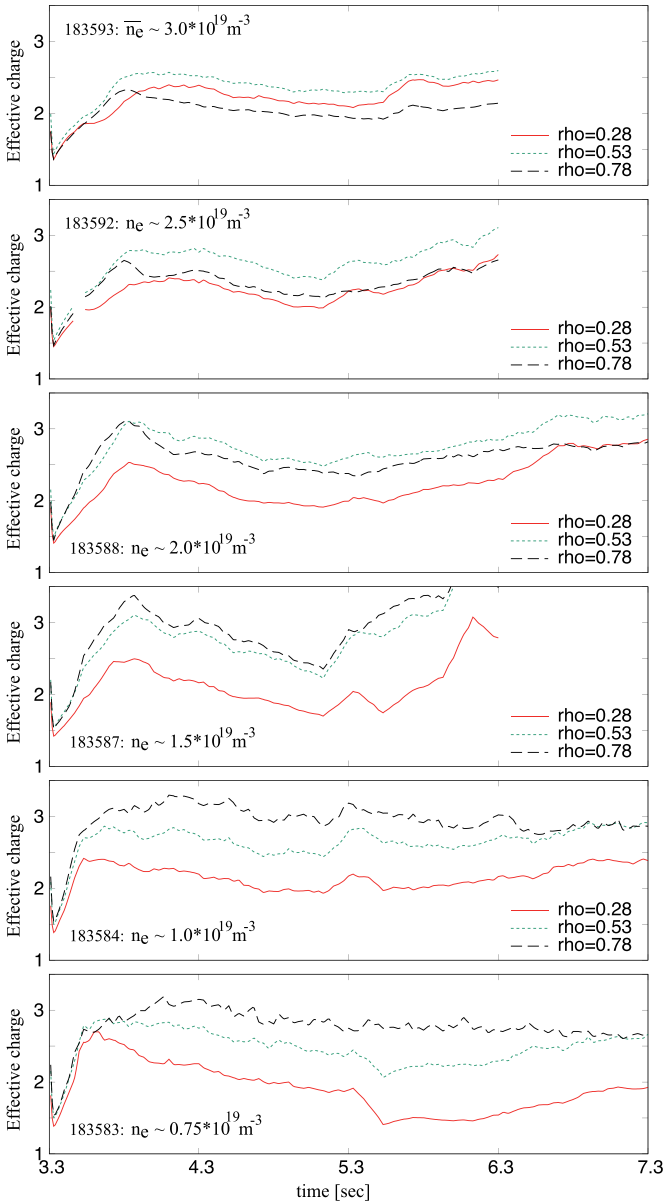
Figure 24. Time evolutions of Z_{eff} at $\rho = 0.28$, 0.53 and 0.78 in the balance injection cases.

dominated by the source term, S (see equation (3)). In contrast, we investigate the effective confinement time in the steady-state (NBs are turned on phase) with the measured n_C profile in this paper. This implies that the effective confinement time in the neutron decay phase may be different in the beam-injected phase. If this is correct, the effective confinement time changes immediately after NB power is changed.

Unfortunately, there are several difficulties in investigating the neutron decay after NBs are turned off. The first is that ECH is turned off at $t = 5.3$ s. The neutron decay after all NBs are turned off is inappropriate for the investigation because the plasma is terminated. Although the neutron decay after the second NB is turned off ($t = 6.3$ s) can be investigated, the difference in the effective confinement time between the second
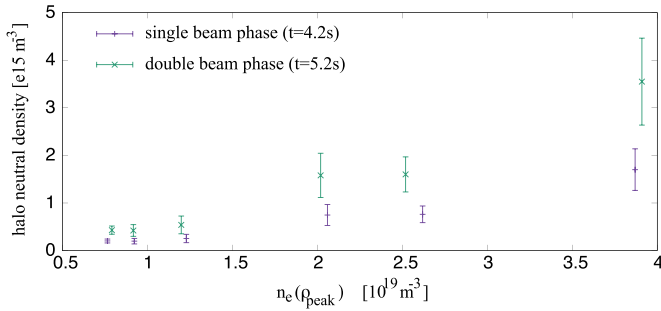
double-beam phase and the second single-beam phase is not large enough. For example, in the SN183594 discharge, these effective confinement times are $\tau_c^{\text{eff}} = 0.082$ s and 0.13 s. It is difficult to estimate this difference in the effective confinement time from the neutron measurement with sufficient accuracy. In contrast, the effective confinement time in the previous short-pulse experiments is $\tau_c^{\text{eff}} \sim 0.5$ s. It is desirable to investigate the neutron decay after all NBs are turned off because estimating the difference between $\tau_c^{\text{eff}} = 0.13$ s to $\tau_c^{\text{eff}} \sim 0.5$ s is relatively easy. To do this investigation, we have to search other series of experiments. Second, the plasma becomes more collisional after ECH is turned off. This makes the confinement time estimation difficult because the collisional slowing down component becomes dominant in the neutron decay process instead of the fast-ion loss. Third, NB#4, used for CXS measurement, is injected each 200 ms. This beam limits the duration that can be used for the neutron decay fitting. This makes the confinement time estimation difficult. For these reasons, the investigation of the change in the effective confinement time before/after NB off is left for future work.

5.2.6. Other candidate. One of the other candidates is the CX loss between fast-ions and halo neutrals. Halo neutrals are generated by CX reactions and populated along the neutral beam path. At first, energetic beam neutrals generate thermal neutrals through the charge exchange reaction to thermal ions. This process is so-called DCX. Next, thermal neutrals generated by DCX interact with thermal ions and yield halo(0) neutrals. After that, halo(i) neutrals yield halo($i + 1$) neutrals again and again. Finally, thermal neutrals are populated along a neutral beam path like a halo.

The CX loss to halo neutrals does not conflict with the following features. First, the number of generated halo-neutral depends on the NB power. This trend is consistent with the confinement degradation depending on the NB power. Second, because the velocity of the halo neutrals is sufficiently slower than that of fast-ions, the CX reactivity is not sensitive to the beam injection direction. Third, with increasing plasma density, more halo neutrals can be supplied because the NB shine-through rate decreases with increasing plasma density.

There are some activities [37, 43, 44] to estimate the halo neutral density in fusion plasmas to apply for the CXS measurement because the neutral density profile in the plasma core region is difficult to measure. Because the generated halo neutrals do not have toroidal or poloidal symmetry, the halo neutral density must be estimated via three-dimensional simulations. Therefore, the analysis of the CX loss of fast-ions to halo neutrals requires a five-dimensional simulation (2D in velocity space and 3D in real space). Although these simulation can be performed by combining GNET [45, 46] and FIDASIM [37, 38], these are left for future work because these simulations are not easy.

Here, we simply estimate the necessary halo neutral density instead of performing detailed simulations. If the CX reaction between a fast-ion and a halo neutral dominates confinement

Figure 25. The halo neutral density estimated by equation (20) with $n_e(\rho_{\text{peak}})$ is shown. The purple and green points indicate the halo neutral densities in the single and double beam phases, respectively.

degradation, the halo neutral density n_0^{halo} satisfies the following expression:

$$\frac{P_{\text{NB}}}{\tau_{\text{ano}}} = n_0^{\text{halo}} \langle \sigma_{\text{cx}} v \rangle. \tag{20}$$

The CX cross-section is given by [47],

$$\sigma_{\text{cx}}(E) = 0.6937 \times 10^{-14} \frac{(1 - 0.155 \log_{10} E)^2}{1 + 0.1112 \times 10^{-14} E^{3.3}}, \tag{21}$$

where E is the fast-ion kinetic energy in eV/amu, and σ_{cx} is in m^2. For simplicity, the relative velocity is assumed to be the beam injection velocity.

Figure 25 shows the halo neutral density estimated by equation (20) with the electron density in the single and double beam phases. If the confinement degradation is governed by the CX loss between a fast-ion and a halo neutral, a halo neutral density of approximately $\sim 10^{14} - 10^{15}$ m^{-3} is needed. Because these values are the flux-averaged densities, the local halo neutral density must be higher than these values.

In the [44], the halo neutral density profile was numerically estimated in LHD for perpendicular hydrogen NB. The beam injection energy was $E_{\text{NB}} \sim 40$ keV and the port through power was $P_{\text{NB}} \sim 4.5$ MW. The line averaged electron density was approximately $\bar{n}_e \sim 0.8 \times 10^{19}$ m^{-3}. In the paper, the halo neutral in the core region was estimated at approximately $n_0 \sim 10^{14} - 10^{15}$ m^{-3}.

Considering that the CX cross-section of the 160 keV deuterium beam is approximately one order less than that of the 40 keV hydrogen beam, it seems that the halo-neutral density generated by the tangential deuterium beam is not sufficient to explain the confinement degradation. Anyway, the detailed estimation is left for future work.

6. Conclusion

We investigated tangential neutral beam fast-ion confinement in MHD quiescent LHD plasmas. To investigate the degradation of the fast-ion confinement, we have performed a series of experiments using deuterium gas and deuterium neutral beams in the LHD. The experimental results show that

the neutron emission rate per beam power decreases as the number of injected tangential beams is increased during a single discharge, as shown in figure 3. The change in the number of injected beams does not have a significant effect on the plasma temperature and density, the NB shine-through rate, or the amplitude of the magnetic fluctuations. Therefore, the fast-ion confinement degradation, which is not caused by MHD instabilities, causes the reduction in the neutron emission rate per beam power. This anomalous degradation of the fast-ion confinement was also observed in discharges with combination of two beams in different directions, as shown in figure 6.

In section 4, we modeled the degradation, which depends on the beam power, to estimate the effective fast-ion confinement time τ_c^{eff} based on the measured data. The obtained effective confinement times are listed in table 1. The results of neutron emission rate simulations performed with TASK/FP code using the obtained effective confinement times are in good agreement with the experimental results as shown in figure 9. Therefore, the effective confinement times obtained with our model are valid in our experimental conditions. In addition, the confinement degradation depends on the electron density, as shown in figure 10.

We estimated the effective confinement time with equation (19) for discharges with combinations of two beams in different directions, because the expression for the confinement degradation, equation (15), can not be applied due to the beam-beam fusion reaction. The results of neutron emission rate simulations for these cases are also in good agreement with the experimental results, as shown in figure 11. This result supports the assumption that the degradation does not depend on the beam direction.

The degradation of the fast-ion confinement leads to a reduction in the NB heating efficiency. The effective confinement times listed in table 1 for single beam heating (~ 2 MW) are shorter than the kinetic energy dissipation time due to the classic deceleration $\tau_{se}/2$ in the whole density range performed in this series of experiments (0.75×10^{19} m$^{-3} < \bar{n}_e < 4 \times 10^{19}$ m^{-3}). This leads to poor NB heating efficiency, as shown in figure 13.

Although we discussed the candidates of the degradation mechanisms in section 5, the degradation mechanism was not clarified. Therefore, it is required to investigate further whether the model derived in this paper can be applied to other conditions. The identification of the degradation mechanism is left for future work.

Data availability statement

The LHD data can be accessed from the LHD experiment data repository. www-lhd.nifs.ac.jp/pub/Repository_en.html.

Acknowledgments

Appendix A. Numerical method

In this paper, the neutron emission rate simulation was performed with VMEC [48], FIT3D [49–52], and TASK/FP [31]. The integrated transport analysis suite TASK3D-a [14] includes VMEC and FIT3D and simulations can be performed by using these codes with the measured data.

A flow of the simulation process is shown in figure A1. First, VMEC code is used to simulate the three-dimensional magnetic equilibrium. At this step, the input data for VMEC are set to be consistent with the mapping equilibrium [53, 54] in LHD. Therefore, though the beam-driven current is not estimated and is not given as an input to VMEC in a rigorous sense, the equilibrium change (such as the magnetic axis position and magnetic surface shape) due to the beam-driven current is 'implicitly' reflected. According to the obtained magnetic equilibrium and measured data, the FIT3D code is used to simulate the NB fast-ion birth profile. At this step, the ionization of the beam neutrals is simulated by HFREYA code, and a uniform effective charge $Z_{\mathrm{eff}} = 3$ is assumed. The MCNBI code is used to simulate the NB fast-ion orbits for a few tens of micro-seconds by using the Monte Carlo method including the NB fast-ion prompt loss and the birth profile broadening due to the finite orbit width effect in the NB fast-ion source term. The TASK/FP code is used to calculate the bounce-averaged relativistic momentum distribution function of fast-ion species by solving the three-dimensional (2D in momentum space and 1D in radial direction) Fokker–Planck equation. At this step, the radial transport of the momentum distribution function is neglected. The details of the neutron emission rate simulation performed with TASK/FP are introduced in appendix A.1.

A.1. Fokker-Planck simulation with measured data

In the TASK/FP code, the momentum distribution function is divided into two components, $f_s = f_s^0 + f_s^1$, where the superscripts 0 and 1 indicate the thermal and non-thermal components and the subscript s indicates the particle species. In this paper, s includes five species: electron, proton, deuteron, helium ion, and carbon ion. The TASK/FP code calculates the time evolution of the f_s^1 component. The thermal component f_s^0 is assumed to be the relativistic Maxwellian,

$$f^0{}_s(p) = \frac{n_s^0}{4\pi m_s^2 c T_s K_2 \left(m_s c^2/T_s\right)} \exp\left(-\frac{m_s c^2 \gamma_s}{T_s}\right), \quad \text{(A.1)}$$

where p is the momentum, $\gamma_s = (1 + p^2/m_s^2 c^2)^{1/2}$, c is the velocity of light, and K_n is the n-th order modified Bessel function of the second kind. The electron temperature is obtained based on the Thomson scattering measurements, and the ion temperature is obtained based on the CXS measurements. The
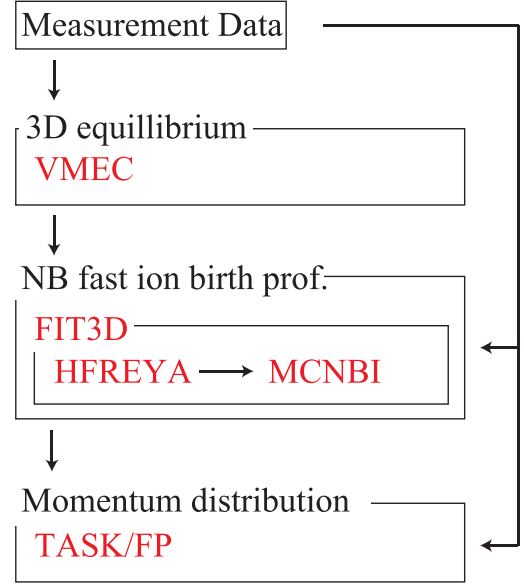

Figure A1. Flow of the neutron emission rate simulation.

electron density of the thermal component n_e^0 is also obtained based on the Thomson scattering measurements. For the ions, the densities of the thermal components are estimated based on the following assumptions and measured data.

The ion densities are governed by the following three expressions:

$$n_P^0 + n_D^0 + n_D^1 + 2n_{\mathrm{He}}^0 + 6n_C^0 = n_e^0 \quad \text{(A.2)}$$

$$\frac{n_D^0 + n_D^1}{n_P^0 + n_D^0 + n_D^1} = r_D \quad \text{(A.3)}$$

$$\frac{n_P^0 + n_D^0 + n_D^1}{n_P^0 + n_D^0 + n_D^1 + n_{\mathrm{He}}^0} = r_H, \quad \text{(A.4)}$$

where subscripts P, D, He, and C indicate the proton, deuteron, helium ion, and carbon ion, respectively. The first, second, and third expressions indicate the charge neutrality, deuteron-proton ratio r_D, and hydrogen-helium ratio r_H. The deuteron-proton ratio and the hydrogen-helium ratio are assumed to be uniform and constant. The typical values used in this series of experiments $r_D = 0.99$ and $r_H = 0.91$ are applied for all discharges. The non-thermal density for deuteron n_D^1 is given by

$$n_D^1 = \int \mathrm{d}\boldsymbol{p}\, f_D^1(\boldsymbol{p}). \quad \text{(A.5)}$$

The carbon density n_C^0 is obtained based on the CXS measurements. In the TASK/FP code, the effective charge Z_{eff} is not given value. Taking into account the n_C^0 profile, the non-uniform and time-evolving Z_{eff} profile can be considered to estimate the neutron emission rate, which is related to Z_{eff}. Figure A2 shows an example of the effective charge profile. In the neutron emission rate simulation, the time evolution of the n_C profile must be included because the variation in Z_{eff} is non-negligible.
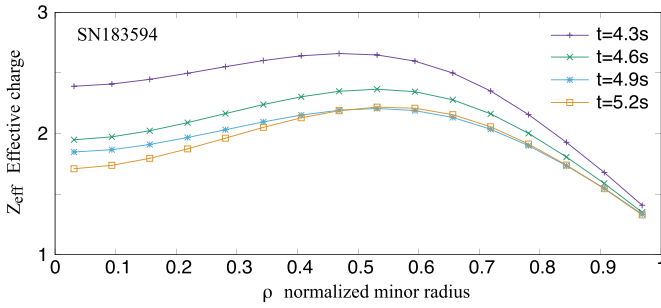
Figure A2. Time evolution of the radial profile of the effective charge for SN183594 is shown.

The evolution of the non-thermal component f_D^1 is described by the Fokker–Planck equation,

$$\frac{\partial f_D^1}{\partial t} = \sum_s C^{D/s}\left(f_D^1, f_s\right) + S_{NB} - L_{eff} - L_{sink} \quad \text{(A.6)}$$

$$C^{D/s}\left(f_D^1, f_s\right) = \nabla_p \cdot \left[\overset{\leftrightarrow}{\boldsymbol{D}}_C^{D/s} \cdot \nabla_p f_D^1 - \boldsymbol{F}_C^{d/s} f_D^1\right] \quad \text{(A.7)}$$

$$L_{eff} = -\frac{f_D^1}{\tau_c^{eff}} \quad \text{(A.8)}$$

$$L_{sink} = -\frac{f_D^1}{\tau_{sink}} \text{ for } |\boldsymbol{p}_D| < 3p_{th,D}, \quad \text{(A.9)}$$

where ∇_p is a derivative operator in momentum space and $C^{D/s}$ is the Coulomb collision term between the incident particle species D and the background particle species *s*. The tensor $\boldsymbol{D}_C$ and the vector $\boldsymbol{F}_C$ are the relativistic non-linear Coulomb collision coefficients given by [55]. The NB fast-ion source term S_{NB} calculated by FIT3D is used as the input. The effective loss term L_{eff} describes the exponential decay of the momentum distribution function with the time constant τ_c^{eff}. The value of τ_c^{eff} for passing particles is given by equation (16) or equation (17) and the value for the trapped particles is chosen to be $\tau_c^{eff} = 0.053$ s [13]. Because we focus on tangential NB fast-ions in this paper, the confinement degradation of trapped particles is not considered. The particle sink term L_{sink} describes the fast-ion sink due to thermalization to prevent the accumulation of thermal ions. The time constant $\tau_{sink} = 1$ ms is an artificial value, and $p_{th,D}$ represents the thermal momentum of the deuterons.

The fusion reaction rate $\mathcal{R}$ at the local point is given by

$$\mathcal{R} = \iint \sigma_{nf}\left(E_{CM}\right) \bar{v} f_D\left(\boldsymbol{p}_a\right) f_d\left(\boldsymbol{p}_b\right) \mathrm{d}\boldsymbol{p}_a \mathrm{d}\boldsymbol{p}_b, \quad \text{(A.10)}$$

where σ_{nf} is the fusion cross-section of D(d,n)^{3}He reaction given by [29], E_{CM} is the kinetic energy in the center of mass frame, and $\bar{v}$ is the relative velocity between two reactant deuterons. Because the beam-beam fusion reaction must be considered in the balance injection case, the fusion cross-section with the beam-thermal approximation [28] is not applied. The neutron emission rate S_n is given by the integration of $\mathcal{R}$ over

the plasma volume. The plasma volume is assumed to be constant in the Fokker–Planck simulation. For this reason, the simulated neutron emission rate has poor agreement immediately after the plasma start-up.

ORCID iDs

H. Nuga ⓘ https://orcid.org/0000-0003-3293-488X
R. Seki ⓘ https://orcid.org/0000-0002-5364-805X
K. Ogawa ⓘ https://orcid.org/0000-0003-4555-1837
H. Yamaguchi ⓘ https://orcid.org/0000-0002-1177-3370
S. Kamio ⓘ https://orcid.org/0000-0003-0755-2433
Y. Fujiwara ⓘ https://orcid.org/0000-0003-2985-060X
Y. Kawamoto ⓘ https://orcid.org/0000-0002-6337-4080
M. Yoshinuma ⓘ https://orcid.org/0000-0002-5113-9710
T. Kobayashi ⓘ https://orcid.org/0000-0001-5669-1937
Y. Takemura ⓘ https://orcid.org/0000-0003-3754-897X
M. Isobe ⓘ https://orcid.org/0000-0002-3572-1882
M. Osakabe ⓘ https://orcid.org/0000-0001-5220-947X
M. Yokoyama ⓘ https://orcid.org/0000-0001-8856-1483

References

[1] Heidbrink W. and Sadler G. 1994 *Nucl. Fusion* **34** 535
[2] Gorelenkov N.N., Pinches S. and Toi K. 2014 *Nucl. Fusion* **54** 125001
[3] Heidbrink W., Collins C., Podestà M., Kramer G., Pace D., Petty C., Stagner L., Van Zeeland M., White R. and Zhu Y. 2017 *Phys. Plasmas* **24** 056109
[4] Takeiri Y. 2018 *IEEE Trans. Plasma Sci.* **46** 1141–8
[5] Takeiri Y. 2018 *IEEE Trans. Plasma Sci.* **46** 2348–53
[6] Osakabe M. *et al* 2017 *Fusion Sci. Technol.* **72** 199–210
[7] Osakabe M., Isobe M., Tanaka M., Motojima G., Tsumori K., Yokoyama M., Morisaki T. and Takeiri Y. 2018 *IEEE Trans. Plasma Sci.* **46** 2324–31
[8] Isobe M. *et al* 2014 *Rev. Sci. Instrum.* **85** 11E114
[9] Isobe M. *et al* 2018 *Nucl. Fusion* **58** 082004
[10] Isobe M. *et al* 2018 *IEEE Trans. Plasma Sci.* **46** 2050–8
[11] Ogawa K. *et al* 2018 *Plasma Phys. Control. Fusion* **60** 095010
[12] Nuga H., Seki R., Ogawa K., Kamio S., Fujiwara Y., Osakabe M., Isobe M., Nishitani T. and Yokoyama M. (LHD Experiment Group) 2019 *Plasma Fusion Res.* **14** 3402075
[13] Nuga H., Seki R., Ogawa K., Kamio S., Fujiwara Y., Osakabe M., Isobe M., Nishitani T. and Yokoyama M. (LHD Experiment Group) 2020 *J. Plasma Phys.* **86** 815860306
[14] Yokoyama M. *et al* 2017 *Nucl. Fusion* **57** 126016
[15] Nuga H., Seki R., Ogawa K., Kamio S., Fujiwara Y., Yamaguchi H., Osakabe M., Isobe M., Murakami S. and Yokoyama M. 2021 *Plasma Fusion Res.* **16** 2402052
[16] Takeiri Y. *et al* 2017 *Nucl. Fusion* **57** 102023
[17] Murase T., Motojima G., Tanaka H., Morisaki T. and Mita M. 2016 *Plasma Fusion Res.* **11** 1205030
[18] Motojima G. *et al* 2019 *Nucl. Fusion* **59** 086022
[19] Takeiri Y. *et al* 2010 *Fusion Sci. Technol.* **58** 482–8
[20] Kaneko O. *et al* 2009 *Plasma Fusion Res.* **4** 027
[21] Kawahata K. *et al* 2010 *Fusion Sci. Technol.* **58** 331–44
[22] Narihara K., Yamada I., Hayashi H. and Yamauchi K. 2001 *Rev. Sci. Instrum.* **72** 1122–5
[23] Yamada I., Narihara K., Funaba H., Minami T., Hayashi H., Kohmoto T. and (LHD Experiment Group) 2010 *Fusion Sci. Technol.* **58** 345–51

[24] Kawahata K., Tanaka K., Ito Y., Ejiri A. and Okajima S. 1999 *Rev. Sci. Instrum.* **70** 707–9

[25] Yoshinuma M., Ida K., Yokoyama M., Osakabe M. and Nagaoka K. 2010 *Fusion Sci. Technol.* **58** 375–82

[26] Chen J., Ida K., Yoshinuma M., Murakami I., Kobayashi T., Ye M. and Lyu B. 2019 *Phys. Lett.* A **383** 1293–9

[27] Ida K., Yoshinuma M., Kobayashi T., Fujiwara Y., Chen J., Murakami I., Kisaki M. and Osakabe M. (LHD Experiment Group) 2019 *Plasma Fusion Res.* **14** 1402079

[28] Mikkelsen D. 1989 *Nucl. Fusion* **29** 1113

[29] Bosch H.S. and Hale G. 1992 *Nucl. Fusion* **32** 611

[30] Strachan J. *et al* 1981 *Nucl. Fusion* **21** 67

[31] Nuga H., Seki R., Kamio S., Ogawa K., Isobe M., Osakabe M., Yokoyama M. and (LHD Experiment Group) 2019 *Nucl. Fusion* **59** 016007

[32] Miyamoto K. 2011 *Fundamentals of Plasma Physics and Controlled Fusion (NIFS-PROC-88)* 3rd edn (National Institute for Fusion Science)

[33] Ogawa K., Isobe M., Nishitani T. and Kobuchi T. 2018 *Rev. Sci. Instrum.* **89** 113509

[34] Ogawa K. *et al* 2021 *Plasma Phys. Control. Fusion* **63** 065010

[35] Heidbrink W., Luo Y., Burrell K., Harvey R., Pinsker R. and Ruskov E. 2007 *Plasma Phys. Control. Fusion* **49** 1457

[36] Fujiwara Y. *et al* 2020 *Nucl. Fusion* **60** 112014

[37] Geiger B. *et al* 2020 *Plasma Phys. Control. Fusion* **62** 105008

[38] Heidbrink W., Liu D., Luo Y., Ruskov E. and Geiger B. 2011 *Commun. Comput. Phys.* **10** 716–41

[39] Tahara K., Asai H., Nuga H. and Murakami S. 2023 *Phys. Plasmas* **30** 082505

[40] Okano K., Suzuki T., Umeda N., Hiwatari R., Masaki K., Tobita K. and Fujita T. 2005 *J. Plasma Fusion Res.* **81** 579–80

[41] Tani K., Honda M., Oikawa T., Shinohara K., Kusama Y. and Sugie T. 2015 *Nucl. Fusion* **55** 053010

[42] Itoh K., Sanuki H. and Itoh S.I. 1992 *Nucl. Fusion* **32** 1047

[43] Medley S., Liu D., Gorelenkova M., Heidbrink W. and Stagner L. 2016 *Plasma Phys. Control. Fusion* **58** 025007

[44] Ito T. *et al* 2010 *Plasma Fusion Res.* **5** S2099

[45] Murakami S. *et al* 2004 *Fusion Sci. Technol.* **46** 241–7

[46] Yamaguchi H. and Murakami S. 2015 *Nucl. Fusion* **56** 026003

[47] Riviere A. 1971 *Nucl. Fusion* **11** 363

[48] Hirshman S.P. and Whitson J. 1983 *Phys. Fluids* **26** 3553–68

[49] Murakami S., Nakajima N. and Okamoto M. 1995 *Trans. Fusion Technol.* **27** 256–9

[50] Sato M., Murakami S., Fukuyama A., Nakamura Y., Watanabe K., Toda S., Yokoyama M., Funaba H., Yamada H. and Nakajima N. 2008 Implementation of nbi heating module fit3d to hierarchy-integrated simulation code TASK3D *Proc. 18th Int. Toki Conf.* (*Ceratopia Toki, Toki Gifu Japan*, *9–12 December 2008*) (available at: www. nifs.ac.jp/itc/itc18/)

[51] Vincenzi P., Bolzonella T., Murakami S., Osakabe M., Seki R. and Yokoyama M. 2016 *Plasma Phys. Control. Fusion* **58** 125008

[52] Seki R., Ogawa K., Isobe M., Yokoyama M., Murakami S., Nuga H., Kamio S., Fujiwara Y. and Osakabe M. (LHD Experiment Group) 2019 *Plasma Fusion Res.* **14** 3402126

[53] Suzuki C., Ida K., Suzuki Y., Yoshida M., Emoto M. and Yokoyama M. 2012 *Plasma Phys. Control. Fusion* **55** 014016

[54] Emoto M. *et al* 2012 *Fusion Eng. Des.* **87** 2076–80

[55] Braams B. and Karney C. 1989 *Phys. Fluid* B **1** 1355–68